Ab initio defect energetics of perovskite (001) surfaces for solid oxide fuel cells: A comparative study of $LaMnO_3$ versus $SrTiO_3$ and $LaAlO_3$

Yueh-Lin Lee[1,2] and Dane Morgan[1,*]

[1]*Department of Materials Science and Engineering, University of Wisconsin-Madison, 1509 University Avenue, Madison, Wisconsin 53706, USA*

[2]*Electrochemical Energy Laboratory and Department of Mechanical Engineering, Massachusetts Institute of Technology, 77 Massachusetts Avenue, Cambridge, Massachusetts, 02139, USA*

(Received 12 February 2014; revised manuscript received 20 March 2015; published 21 May 2015)

In this paper, we perform a comparative study based on *ab initio* modeling for perovskite ABO_3 (001) surfaces and surface defect energetics in order to understand the influence of polarity and redox active Mn in the $LaMnO_3$ system. We consider $LaMnO_3$, $LaAlO_3$, $SrTiO_3$, and briefly $LaFeO_3$ systems for comparison, which illustrate the interplay between properties of polar surfaces and the varying d-electron shell of transition metals. We are motivated by the need to understand the surfaces of mixed electronic and ionic conductors typically used in solid oxide fuel cell cathodes and other ion conducting technologies, which are represented here by the $LaMnO_3$ system. We focus on the influence of the metal character and surface polarity on the surface and surface defect chemistry in these selected systems. We demonstrate that the facile redox of the TM ($3d^4$) in $LaMnO_3$ with partial e_g orbital occupation (or specifically e_g occupancy close to 1) allows the polar surfaces to be compensated by changes in charge density over relatively short length scales (3 to 4 unit cells or ~1.5 nm) near the surface as compared to $LaAlO_3$. In contrast to $LaAlO_3$, this low-energy and short-range screening mechanism leads to low surface energies without any additional reconstruction, rapidly converging surface properties with film thickness (by ~8 unit cells), bulklike defect chemistry more than ~1.5 nm from the surface, and surface defect energetics that are primarily governed by the local charge doping or the created electric field near the polar surfaces. We show that $LaMnO_3$ exhibits very different surface properties from $LaAlO_3$ and $SrTiO_3$, thereby demonstrating that these properties are due to the presence of the redox active transition metal with partial e_g orbital occupation and a polar surface, respectively. These understandings can help guide qualitative analysis, computational study, and design of surfaces of mixed electronic and ionic conductors.

DOI: 10.1103/PhysRevB.91.195430 PACS number(s): 82.47.Ed, 68.47.Gh, 61.72.J−, 73.20.Hb

I. INTRODUCTION

Transition metal (TM) perovskite mixed ionic-electronic conductors are widely used as solid oxide fuel cell cathodes, among a number of other applications [1,2]. $(La_{1-x}Sr_x)MnO_3$ (LSM) is presently a widely used choice of the cathode material in commercial solid oxide fuel cells due to its good electrical conductivity, good stability, reasonable catalytic activity for the oxygen reduction reaction, thermal expansion properties, and relatively low cost [2,3]. Point defects, including ionic and electronic defects, play a crucial role in the oxygen reduction reaction activity of perovskite type mixed ionic-electronic conductors, as both ionic/electronic conductivity and oxygen surface exchange are strongly influenced by the content of point defects in perovskite type mixed ionic-electronic conductors [2,4–6]. The dominant charge carriers in LSM (for $x \leqslant 0.5$ in LSM) are electron holes in the entire oxygen partial pressure region before decomposition [7,8], while the low oxygen vacancy concentration in bulk LSM leads to poor ionic conductivity under most conditions. The low oxygen vacancy concentration distinguishes LSM from most other cathode materials, which have higher oxygen vacancy concentrations and therefore allow transport oxygen through their bulk during their operation in a solid oxide fuel cell cathode [2]. It is generally assumed that transport along a surface path plays a critical role in the LSM cathodic reaction rate, although at high over potential the substantially reduced LSM can create a large content of oxygen vacancies and the bulk path will become colimiting [2,9]. Although understanding of the LSM bulk defect chemistry under solid oxide fuel cell conditions (900–1200 K in air) has been improved over the last two decades [8,10–15], surface defect chemistry, which is critical to oxygen reduction reaction performances [4,5], still remains largely unknown. This limited knowledge is due to difficulties in characterizing perovskite surfaces and the sensitivity of the chemistry to processing history and operating conditions. For example, in various experimental papers [16–24], researchers have reported Sr surface enrichment/segregation on LSM surfaces under polarization or change of oxygen partial pressure or temperature. Factors leading to surface Sr enrichment/segregation, however, still remain unclear and potentially include elimination of surface charge/polarity [25], electrostatic interaction between Sr and oxygen vacancies [20,24], surface strain relaxation [24,26], demixing [27], and potentially other factors. In addition, it is well known that $LaMnO_3$ and LSM can exhibit substantial cation vacancy content (correspond to oxygen overstoichiometry) under typical solid oxide fuel cell operating conditions, and almost nothing is known about how cation vacancies may behave near LSM surfaces. Hence, a detailed picture of surface defect chemistry remains largely unresolved. Furthermore, while we here focus on $LaMnO_3$ as a representative of the LSM system, other TM-based mixed ionic-electronic conducting oxides [e.g., $(La_{1-x}Sr_x)CoO_3$ [28,29] and $(La_{1-x}Sr_x)(Co_{1-y}Fe_y)O_3$ [30,31]] are being explored for

*Corresponding author: ddmorgan@wisc.edu

solid oxide fuel cells, and similar uncertainty to that in LSM exists about their surface defect chemistry. The present studies focus on general trends associated with the surface energetics and TM properties, particularly for TM-based mixed ionic-electronic conducting perovskites with an e_g orbital degeneracy, which exhibit energetically facile redox capability, and are commonly used in solid oxide fuel cell cathode applications.

A number of *ab initio* studies have been performed on perovskite (001) surfaces. These studies have led to a good understanding of surface reconstruction stabilization mechanisms for polar surfaces of ionic-based oxides [32–35]. However, as we will show in this paper, different stabilization mechanisms can occur in mixed ionic-electronic conducting oxide polar surfaces, as the energetic cost of surface charge doping in mixed ionic-electronic conductors is comparable to or lower than the change of surface stoichiometry. Within the family of TM-based mixed ionic-electronic conducting perovskites, there have also been a range of *ab initio* studies of perovskite surfaces, primarily (001) surfaces, including for the LSM system. In particular, a number of studies have addressed the defect energetics of AO and BO_2 terminate surfaces. For example, Lee *et al.* showed that the oxygen vacancy formation energy in $LaMnO_3$ is about 1 eV lower (higher) than the bulk value for BO_2 (AO) terminated surfaces [36,37]. Similar results were found by Kotomin *et al.* [38] and Piskunov *et al.* [39] for $LaMnO_3$/LSM, and similar trends have been found for other TM systems [e.g., $LaCoO_3$/(La,Sr)CoO_3 [36,40]]. A few studies have also looked at cation defect energetics, although almost entirely focused on Sr or dopant segregation rather than cation vacancies [19,20,24,29,41]. These studies have found that Sr segregation is coupled with the change of oxygen chemical potential (temperature and oxygen partial pressure), although opposite oxygen partial pressure dependences on surface Sr segregation were both reported, e.g., Refs. [19,20,29] vs Ref. [24].

While previous studies have established that defect energetics are different at the surfaces of many perovskites, there is still an insufficient understanding of what the mechanisms driving these differences between TM and other non-TM systems are, of how these mechanisms differ and lead to different surface chemistry, and of how these mechanisms relate to fundamental factors such as nature of metal-ligand field and polar surface compensation. Such understanding is important for robust modeling, experimental interpretation, and material design relating to surfaces and interfaces of these materials.

In this paper, we present detailed investigations of surface defect energetics for $LaMnO_3$ (001) polar surfaces, including oxygen vacancies, cation vacancies, and Sr (Ca and Ba) doping. Two other canonical examples of ABO_3 perovskite (001) surfaces, $SrTiO_3$ and $LaAlO_3$, are also included to serve as comparative cases to highlight the fundamentally different metal-ligand characteristics for surface defect behavior of $LaMnO_3$/LSM, as well as to understand the role of polarity and redox active TMs on the surface defect energetics. We note that this paper is not intended for investigating surface defect chemistry of $LaAlO_3$ and $SrTiO_3$, which, due to their significant band gaps, require significantly more efforts to treat defect charge states, band gap error in density functional theory (DFT), surface space charge, etc. Such studies are beyond the scope of this paper. Instead, only results of slab calculations in $LaAlO_3$ and $SrTiO_3$ that are similar to those we discuss in $LaMnO_3$ are considered, as these are essential for comparison and are useful for understanding of the influence of redox active Mn and polarity on $LaMnO_3$ surface defect energetics.

Due to complexity as well as a lack of experimental information on $LaMnO_3$/LSM surface reconstructions, in this paper we focus on surfaces constructed through simply cleaving the bulk and allowing for only local relaxations within fixed size supercells. This approach does not allow for significant atomic rearrangements, which might be separated by a barrier from the cleaved surface, nor reconstructions that might be incommensurate with our unit cell. However, these surfaces are adequate to compare mechanisms of charge accommodation of surface polarity vs surface defect energetics among the different systems, which is the focus of this paper. We note that while these cleaved surfaces are certainly oversimplified for $LaAlO_3$ [33,34] and $SrTiO_3$ [35], it is quite possible that these are the correct surface for LSM/$LaMnO_3$. These surfaces have been predicted to be a possible stable surface structure [39,42,43] under solid oxide fuel cell operating conditions and have been found experimentally for similar systems both at low temperature and high temperature in recent studies [44–47]. This paper demonstrates how facile charge motion can stabilize $LaMnO_3$/LSM surface without significant atomic reconstruction, thereby further supporting the use of these ideal surfaces. Furthermore, these simple surfaces have been widely and successfully used to model perovskite surface activities [48–50] as well as LSM surface Sr segregation [24], which provides additional support for their relevance to both modeling and catalytic activity. Although there have been theoretical studies in the literature focusing on surface properties of each of these perovskite systems individually [24,32,39,51–55], we here provide our own set of comprehensive calculations rather than relying on previous studies. These repeated calculations are necessary as the calculated surface properties may vary depending on the adopted computation approaches or modeling methods (e.g., slab thickness, symmetric vs asymmetric slab models), which add difficulty/uncertainty in comparing different theoretical papers reported in the literature. Our systematic study for unreconstructed (001) surfaces of the three representative perovskites using consistent computational modeling approaches provides a consistent set of data for distinguishing key factors that govern perovskite surface properties from material perspectives.

This paper is organized as follows. Section II describes our *ab initio* modeling approach. Section III discusses results of calculated $LaAlO_3$, $SrTiO_3$, $LaMnO_3$ (001) surface electronic structures, charge doping, slab electrostatic potential profiles; and surface energies. These calculations provide clear evidence of how $LaMnO_3$ surface properties are distinct from $LaAlO_3$ and $SrTiO_3$. Section IV discusses surface segregation energetics for point defects and dopants for $LaMnO_3$ (001) surfaces vs $LaAlO_3$, $SrTiO_3$, where it is demonstrated that only $LaMnO_3$ exhibits a correlation between surface dipole compensating charge and surface point defect segregation energies normalized with respect to the point defect charge. Section V summarizes the key results and fundamental factors

TABLE I. Calculated bulk lattice constants, Bader charge, and bulk defect formation energies of $LaAlO_3$, $SrTiO_3$, and $LaMnO_3$ in this paper.

Lattice constant, a_p (Å)	$LaAlO_3$ $a_{LaAlO3} = 3.816$			$SrTiO_3$ $a_{SrTiO3} = 3.931$			$LaMnO_3$ $a_{LaMnO3} = 3.941$		
Bader charge	La	Al	O	Sr	Ti	O	La	Mn	O
	2.043	3.000	–1.681	1.595	2.207	–1.266	2.076	1.728	–1.268
Defect formation energy (eV)	V_A'''	V_B'''	$V\ddot{o}$	V_A''	V_B''''	$V\ddot{o}$	V_A''' (Sr_A')	V_B'''	$V\ddot{o}$
$E_{bulk}(def) + E(i) - E_{bulk}$(perf) in the A-site metal oxide rich condition	$La_2O_3/LaAlO_3/O_2$ equilibrium			$SrO/SrTiO_3/O_2$ equilibrium			$La_2O_3/LaMnO_3/O_2$ equilibrium		
	2.5	3.2	6.8	2.3	3.3	5.40[a] 5.57[b]	–0.2 (−1.2)[c]	–1.1	3.6[c] 3.9[c]
$E_{bulk}(def) + E(i) - E_{bulk}$(perf) in the B-site metal oxide rich condition	$Al_2O_3/LaAlO_3/O_2$ equilibrium			$TiO_2/SrTiO_3/O_2$ equilibrium			$Mn_2O_3/LaMnO_3/O_2$ equilibrium		
	2.1	3.6	6.8	1.0	4.6	5.40[a] 5.57[b]	–0.6 (−1.6)[d]	–0.7	3.6[c] 3.9[d]

[a] $V\ddot{o}$ in the AO plane of the $2 \times 2 \times 8$ perovskite supercell (the AO plane is defined perpendicular to the z direction).
[b] $V\ddot{o}$ in the BO_2 plane of the $2 \times 2 \times 8$ perovskite supercell (the BO_2 plane is defined perpendicular to the z direction).
[c] The chosen $E(i)$ reference for Sr_{La} doping is $[E(SrO) - 1/2 \bullet E(O_2)] - 1/2 \bullet [E(La_2O_3) - 3/2 \bullet E(O_2)]$.
[d] The chosen $E(i)$ reference for Sr_{La} doping is $[E(SrO) - 1/2 \bullet E(O_2)] - [E(LaMnO_3) - 1/2 \bullet E(Mn_2O_3) - 3/2 \bullet E(O_2)]$.

leading to distinct behavior for the $LaMnO_3$ surface properties shown in this paper, and finally Sec. VI gives the conclusions.

II. *AB INITIO* CALCULATION APPROACH

Calculations were performed with the Vienna *Ab initio* Simulation Package (VASP) [56,57] using DFT and the projector augmented plane wave (PAW) method [58,59]. Exchange correlation was treated in the Perdew-Wang-91 (PW-91) [60] generalized gradient approximation (GGA). The Brillouin zone was sampled by a Monkhorst-Pack k-point mesh of $4 \times 4 \times 4$ for a five atom perovskite unit cell. Energy convergence with respect to k-points was better than a 3 meV per perovskite formula unit. Octahedral distortion in perovskites is included by using $2a_p \times 2a_p \times 2a_p$ supercells, with internal relaxation starting from experimental symmetry for $LaAlO_3$ [61], $SrTiO_3$ (with no octahedral distortion) [62], and $LaMnO_3$ [63], where a_p is the DFT-based lattice constant of an ideal perovskite unit cell (summarized in Table I below).

Standard DFT-GGA calculations were performed in the cases of $LaAlO_3$ and $SrTiO_3$ (001) surfaces, while GGA + U calculations with an effective U (U_{eff}) of 4 eV (fit to the experimental oxidation enthalpy of binary oxides [36,64]) was used for the Mn 3d electrons in the $LaMnO_3$ system. The use of GGA + U has been shown to improve the accuracy of $LaBO_3$ energetics over just GGA [15,36]. Since DFT with the standard GGA level has been shown to provide good description on $SrTiO_3$ formation energies from binary oxides [65] and Ti-based oxide chemistry [66], in this paper we did not employ Hubbard U correction for calculating the $SrTiO_3$ system; therefore, the band gap of $SrTiO_3$ calculated with GGA is underestimated (this is the same for $LaAlO_3$). Improved band structures can be further obtained with DFT + U or hybrid-functional and Green-CoulombGW calculations (at higher computational cost). However, in this paper we take these two systems only as comparative cases, and therefore do not make an effort to correct the band gap deficiency. Both $LaAlO_3$ and $SrTiO_3$ preserve their insulating and semiconducting nature, respectively, as well as their polar character, despite their underestimated band gaps. The standard DFT-GGA approach is thereby suitable for our goals here, which are to investigate trends in defect energetics relative to the bulk of polarized and weakly polarized surfaces for TM and non-TM oxide systems.

Table I lists calculated bulk lattice constant, Bader charges [67] of metal and oxygen constituents, and point defect formation energy of bulk $LaAlO_3$, $SrTiO_3$, and $LaMnO_3$. Figure 1 shows the total density of states (DOS) normalized as per formula unit of bulk $LaAlO_3$, $SrTiO_3$, and $LaMnO_3$. These DOS are in agreement with previously reported DFT-based band structures of $LaAlO_3$, $SrTiO_3$, and $LaMnO_3$ [34,36,52]. Note in this paper that $LaMnO_3$ is more metallic than the ground state $LaMnO_3$ [which is in the A-type antiferromagnetic state and contains Jahn-Teller (JT) distortion for the local Mn-O environment] due to the adopted ferromagnetic state and the constrained structure we apply. The constraints therefore mimic the $LaMnO_3$ and LSM properties under solid oxide fuel cell conditions [15,36] and represent the mixed ionic-electronic conductor character of $LaMnO_3$. We note that the DOS plots in Fig. 1 show a relative low resolution in the energy axis, which is due to low k-point sampling in the DFT calculations. The main purpose of the DOS plots in Fig. 1 in this paper is for comparison with the DOS of the slabs, where the calculations using a large k-point mesh are too computationally demanding. In Fig. 24 (in the Appendix), we provide the DOS of bulk $LaMnO_3$, $LaAlO_3$, and $SrTiO_3$ calculated with a finer k-point mesh, where the main characteristics of the electronic structure near the Fermi level are consistent with those shown in Fig. 1 ($LaMnO_3$ is metallic, while both $LaAlO_3$ and $SrTiO_3$ contain a band gap). We also note that the Fermi level in this paper refers to the zero-temperature Fermi level output by VASP, which is just the energy of the highest occupied electronic state.

Surface calculations were performed using periodic slab models with a 10 Å vacuum placed between the truncated (001) surfaces. Two slab models were included in this paper: (1) symmetric slabs (where both surfaces have the

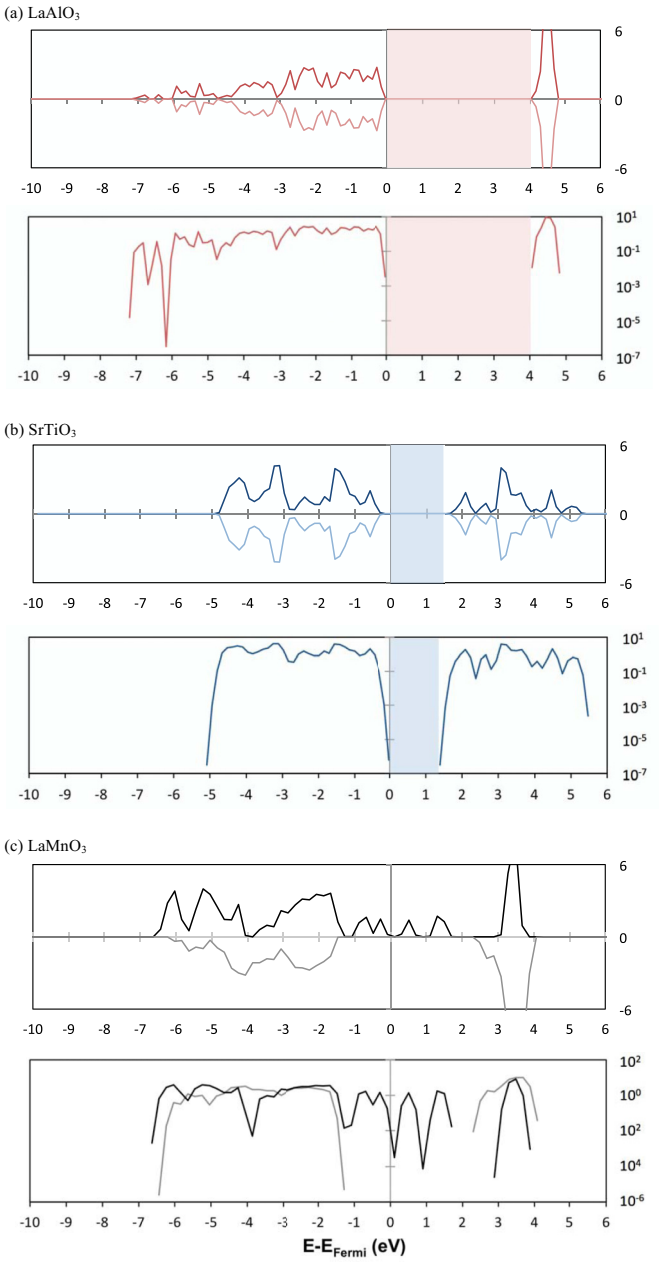

FIG. 1. (Color online) Plots of calculated total DOS (normalized as per formula unit) for bulk (a) $LaAlO_3$, (b) $SrTiO_3$, and (c) $LaMnO_3$. For each material system, two sets of DOS plots with different y axis presentation are included. The upper plot gives absolute y axis with positive numbers for up-spin states and negative numbers for down-spin states and the lower plot gives the logarithm scale y axis with deep color for the up-spin states and light color for down-spin states. The logarithm scale plots exclude zero states in the DOS, which allows one to easily distinguish systems with and without band gaps. In each plot, the Fermi energy level is aligned at zero, and the shaded area represents the size of the band gap.

same termination) and (2) asymmetric slabs (where the system has two different surfaces). In the symmetric slab model, two sets of calculations are needed for the two types of the (001) surface terminations (AO and BO_2). In-plane surface area is set to 2×2 perovskite unit cells for both the symmetric and

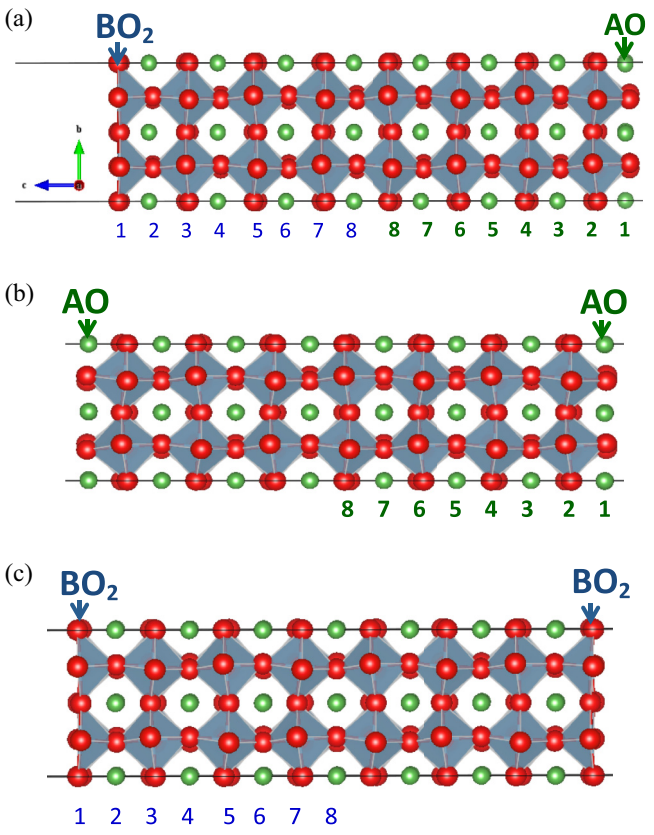

FIG. 2. (Color online) The slab models used in this paper for simulating perovskite (001) surfaces (a) asymmetric (stoichiometric) slab with the AO and BO_2 terminations, (b) symmetric AO terminated slab, and (c) symmetric BO_2 terminated slab. Octahedral rotation (due to ionic radii mismatch) is included in these slab models.

asymmetric slab models. All the slab models are illustrated in Fig. 2. For asymmetric slabs, dipole corrections [68,69] are applied to correct the error from interaction between two surfaces through vacuum via the artificial macroscopic field resulting from periodic boundary conditions.

All bulk $LaAlO_3$, $SrTiO_3$, and $LaMnO_3$ defect calculations were performed with supercells of the same or similar thickness of the slab calculations in order to cancel artificial defect interactions in both slab and bulk calculations. By using the bulk supercell with the same size as the slab model (slab without vacuum space), the lower symmetry in the bulk supercell may lead to different defect formation energy at symmetry distinct lattice sites (e.g., bulk O vacancy formation energy in $SrTiO_3$ and $LaMnO_3$). In the following discussions, we note that the slab point defect segregation energies, $E_{\mathrm{seg}}(def)$s, are calculated by referencing the bulk defect formation energies at the same local symmetry, i.e., the BO_2 (AO) layer defect formation energy in the slab is referenced to the bulk BO_2 (AO) plane defect formation energy, for better cancellation of spurious defect interaction in the finite size supercell calculations between bulk and slabs. In symmetric slab models, point defects are created on one side of slab (with dipole corrections [68,69]) instead of adopting symmetric defect containing slab configurations. All defect calculations in this paper are done for neutral defects, by which

it is meant that the *ab initio* cells used in the calculations are charge neutral. This approach is fully appropriate for the $LaMnO_3$ system under solid oxide fuel cell conditions, which is close to metallic at higher temperatures [70] and high oxygen partial pressure (e.g., ambient air condition) due to self-doping by cation vacancies [71] and does not produce various charged defect states for oxygen vacancies and cation vacancies. In fact, only the neutral point defect species are included in most of the developed bulk $LaMnO_3$ defect models in the literature [8,10–15]. However, for the insulating $LaAlO_3$ and semiconducting $SrTiO_3$ systems, additional charged defect states are possible depending on Fermi level [72,73]. To keep the calculations tractable and to best illustrate differences between the $LaAlO_3$, $SrTiO_3$, and $LaMnO_3$ systems, we exclude these additional charge states. The calculations for defects in $LaAlO_3$ and $SrTiO_3$ are fully correct for the physics of the defects in the otherwise pristine system, with no additional intrinsic or extrinsic defects.

Surface defect segregation energies, $E_{\text{seg}}(def)$, where "*def*" defines which type of point defects, i.e., O vacancy ($V\ddot{o}$ based on the Kröger-Vink notation; the same for the following point defects), *A*-site vacancy (V_A''' in $LaAlO_3/LaMnO_3$ and V_A'' in $SrTiO_3$), *B*-site vacancy (V_B''' in $LaAlO_3/LaMnO_3$ and V_B'''' in $SrTiO_3$), or Sr dopant (Sr_A' in $LaMnO_3$) is used in the DFT calculations, are calculated with the equation

$$E_{\text{seg}}(def) = [E_{\text{slab}}(def(l)) + E(i) - E_{\text{slab}}(perf)] - [E_{\text{bulk}}(def) + E(i) - E_{\text{bulk}}(perf)]. \quad (1)$$

Here $E_{\text{slab}}(def(l))$, $E_{\text{slab}}(perf)$, $E_{\text{bulk}}(def)$, and $E_{\text{bulk}}(perf)$ are the calculated total energy of a slab with a point defect in the l^{th} layer (first layer is the surface layer), the calculated total energy of a perfect slab, the calculated total energy of a bulk supercell with a point defect, and the calculated total energy of a perfect bulk, respectively. $E(i)$ (i = La, Sr, Al, Ti, Mn, and O) is the *ab initio* reference energy of metal cations and oxygen, as defined as follows. At a given oxygen partial pressure and temperature, which sets the chemical potential of oxygen, there are two other degrees of freedom for the chemical potentials of metals in perovskites. By using the calculated *ab initio* total energy of perovskites as a constraint, one independent degree of freedom is still left, and the chemical potential references for the metal constituents cannot be uniquely determined [74]. Therefore, we consider the two boundary conditions for the metal chemical potentials in the oxygen rich environment: (1) *A*-site metal rich condition where the perovskites are in equilibrium with the *A*-site metal binary oxides ($LaAlO_3/La_2O_3/O_2$, $SrTiO_3/SrO/O_2$, and $LaMnO_3/La_2O_3/O_2$ equilibrium) and (2) *B*-site metal rich condition where the perovskites are in equilibrium with the *B*-site metal binary oxides ($LaAlO_3/Al_2O_3/O_2$, $SrTiO_3/TiO_2/O_2$, and $LaMnO_3/Mn_2O_3/O_2$ equilibrium). At these two boundary conditions, the chemical potentials of metals of perovskites are uniquely defined. For example, at the $LaMnO_3/La_2O_3/O_2$ equilibrium, $\mu^0_{LaMnO_3}(La) = {}^1/_2 E^{DFT}_{La_2O_3} - {}^3/_4 E^{DFT}_{O_2}$, $\mu^0_{LaMnO_3}(Mn) = E^{DFT}_{LaMnO_3} - \mu^0_{LaMnO_3}(La) - {}^3/_4 E^{DFT}_{O_2}$, and $\mu^0_{LaMnO_3}(O) = {}^1/_2 E^{DFT}_{O_2}$. Here $\mu^0_{LaMnO_3}(La)$, $\mu^0_{LaMnO_3}(Mn)$, and $\mu^0_{LaMnO_3}(O)$ are the chemical potentials of La, Mn, and O in the $LaMnO_3$ perovskite, respectively, and $E^{DFT}_{LaMnO_3}$, $E^{DFT}_{La_2O_3}$, and $E^{DFT}_{O_2}$ are the calculated DFT total energy of $LaMnO_3$, La_2O_3, and O_2, respectively. $E^{DFT}_{O_2}$ contains an energy correction fit with the formation energy of binary metal oxides as in Ref. [36], which corresponds to the standard condition of 1 atmosphere oxygen partial pressure at room temperature. We note that in order for the perovskite oxides to remain stable relative to the constituent metal binary oxides, the chemical potentials of metals are confined within the two boundary conditions. The specified equilibrium conditions allow one to constrain the metal chemical potential references and hence the point defect formation energies of the metal cations. The bulk values of the point defect formation energies, $[E_{\text{bulk}}(def) + E(i) - E_{\text{bulk}}(perf)]$, at the two specified boundary conditions are provided in Table I.

III. PROPERTIES OF PEROVSKITE (001) SURFACES

A. Bader charge doping of layers for $LaAlO_3$, $SrTiO_3$, and $LaMnO_3$ (001) surfaces

The calculated charge changes of each layer (surface layer charge relative to the bulk layer charge) for $LaAlO_3$, $SrTiO_3$, and $LaMnO_3$ (001) surfaces based on Bader charge analysis [67] are provided in Fig. 25 in the Appendix. Our $LaAlO_3$ and $SrTiO_3$ surface charge results are in agreement with previous theoretical works [54,75,76] except that overall the Bader charge analysis in this paper exhibits smaller magnitude of charge density changes as compared to the results of Mulliken charge analysis.

Due to bulk polarity [32], all the $LaAlO_3$, $SrTiO_3$, and $LaMnO_3$ (001) surfaces are effectively charge doped (see Fig. 25 in the Appendix), with holes created near the BO_2 surfaces and electrons formed near the AO surfaces, except for the $LaAlO_3$ 16-layer asymmetric slab model, where surface lattice polarization occurs to screen the electrical field in the slab along with a minor amount of charge transfer between the AO and BO_2 surfaces [54,77]. In contrast to $LaAlO_3$, lattice polarization does not occur in the $LaMnO_3$ (001) 16-layer asymmetric slabs: both $LaMnO_3$ 16-layer asymmetric and 15-layer symmetric slab models exhibit almost identical surface charge doping, as shown in Fig. 25(c) in the Appendix. That the layer charge of $LaMnO_3$ (001) and the 16-layer symmetric slab is similar to that of the 15-layer symmetric slabs suggests that the $LaMnO_3$ (001) 16-layer slab model has extra surface charge introduced to the (001) surfaces to accommodate the total dipole moment of the slab. Such difference in surface charge compensation between the $LaMnO_3$ and $LaAlO_3$ 16-layer (001) slabs reflects that the facile redox of Mn in $LaMnO_3$ allows it to accommodate extra charge doping at a low-energy cost, while introducing charge to $LaAlO_3$ is energetically unfavorable; therefore, surface stabilization with charge is substituted by lattice polarization in the slab at low thickness.

In the case of weak polar $SrTiO_3$ (001) surfaces, the similarity of layer charge doping between the 16-layer asymmetric and 15-layer symmetric slab models can be attributed to the fact that surface bond breaking on its own is sufficient to compensate the weak polarity [32], and thereby the surface charge doping is mainly a result of local bond breaking near the surface region instead of a macroscopic dipole effect (which leads to the $LaMnO_3$ surface charge). Nonetheless, slight layer

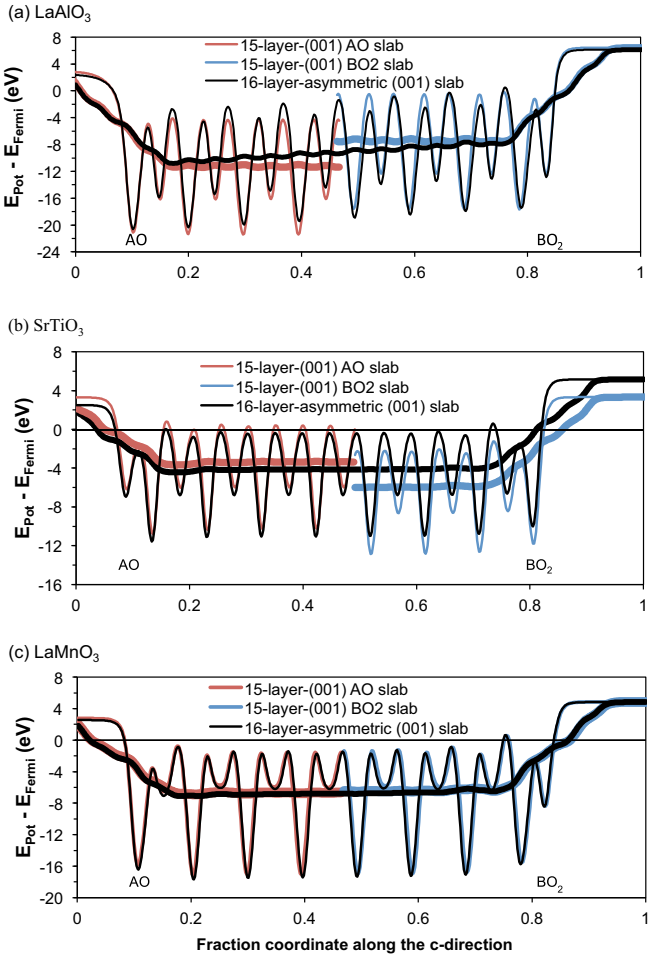

FIG. 3. (Color online) Macroscopic average (thick line) and microscopic average (thin line) electrostatic potential profiles (relative to the Fermi level of the slabs) along the direction perpendicular to the surfaces of the (001) slab models for the perovskite (a) $LaAlO_3$, (b) $SrTiO_3$, and (c) $LaMnO_3$. The black lines are the electrostatic potential profiles of the 16-layer asymmetric slab models, while the blue and red lines are the electrostatic potential profiles of the 15-layer (001) BO_2 and (001) AO slabs, respectively.

charge differences are observed in Fig. 25(b) of the Appendix for the top surface layer between the 16-layer asymmetric and 15-layer symmetric slab models, suggesting that a certain degree of electronic redistribution between the two surfaces may still occur in the asymmetric slab models.

B. Electrostatic potential through the $LaAlO_3$, $SrTiO_3$, and $LaMnO_3$ (001) slabs

To further demonstrate distinct surface properties of $LaMnO_3$ vs $LaAlO_3$ and $SrTiO_3$, in Fig. 3 we show the calculated macroscopic average [78] and microscopic average electrostatic potential (relative to the Fermi level, E_{Fermi}) along the direction perpendicular to the slab surfaces. Among the three perovskite systems, only the $LaMnO_3$ slabs [Fig. 3(c)] exhibit almost the same electrostatic potential profile across the slab between the 16-layer asymmetric (black lines) and 15-layer symmetric slab (blue and red lines) models, suggesting that both the $LaMnO_3$ 15-layer symmetric and 16-layer asymmetric (001) slabs have converged with respect to thickness and contain a bulklike region between the two surface terminations. On the other hand, distinct electrostatic potential profiles can be clearly seen between the $LaAlO_3$ (001) slab 15-layer symmetric and 16-layer asymmetric (001) slabs. Furthermore, despite weak polarity of the $SrTiO_3$, the electrostatic potential profiles of the $SrTiO_3$ (001) symmetric and asymmetric slabs also show clear differences: there is a downshift of the valleys of the electrostatic potential profiles from the 15-layer symmetric (001) AO slab, to the 16-layer asymmetric (001) slab, to the 16-layer symmetric BO_2 slab as the lowest, which indicates the three slab models contain different Fermi levels when one aligns their core-level energies. As will be discussed below in %Sec. III C 2, the difference in the Fermi level of the three slab models are due to the existence of the (001) BO_2 (i.e., TiO_2) surface states, which pins the Fermi level of the slabs containing the (001) BO_2 (TiO_2) termination(s), and charge transfer between the (001) AO (SrO) and BO_2 (TiO_2) terminations of the 16-layer slab models originated from the empty d-shell configuration of $SrTiO_3$, which leads to a band gap in $SrTiO_3$.

C. Electronic structures of perfect (001) surfaces

1. *Polar $LaAlO_3$ (001) surfaces*

Figure 4 shows the DOS plots of $LaAlO_3$ (001) asymmetric (stoichiometric) 16-layer slab and symmetric (nonstoichiometric) BO_2 as well as AO terminated 15-layer slabs compared to the bulk DOS (represented with a thin gray line in each plot). Although all three $LaAlO_3$ (001) slab models exhibit metallization of their surfaces, distinct band structures are clearly observed in their DOS plots.

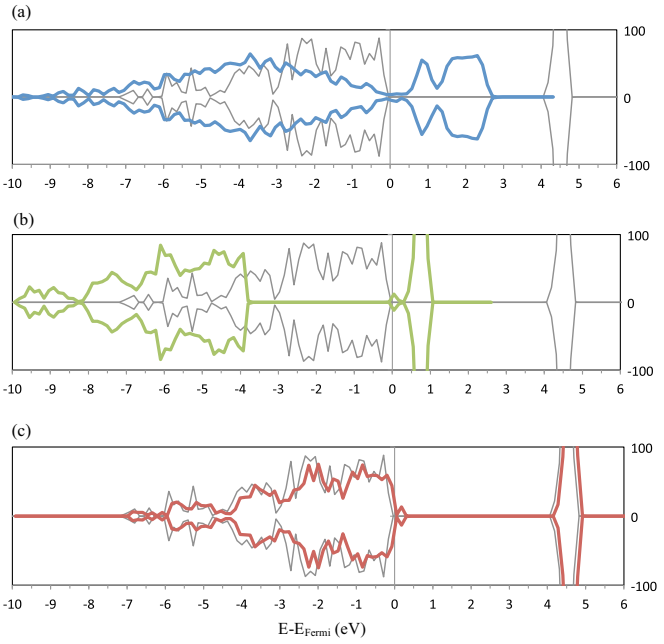

FIG. 4. (Color online) Plots of calculated DOS for $LaAlO_3$ (a) asymmetric 16-layer-slab, (b) symmetric 15-layer-AO-terminated slab, and (c) symmetric 15-layer-BO_2-terminated slab. In each plot, thick and thin solid lines represent the slab and the bulk DOS respectively, and the Fermi energy level is aligned at 0.

For the 16-layer asymmetric slab model [Fig. 4(a)], the more dispersed band structure compared to the bulk [Fig. 1(a), where values for the slab extend almost 3 eV below those of the bulk] is due to band bending or alignment of the Fermi level between the two opposite surfaces (similar results are also shown in Fig. 6 of Ref. [54]), which can also be observed in the slab electrostatic potential profile shown in Fig. 3(a). As discussed previously in Sec. III A, the built-in electric field in the relaxed 16-layer asymmetric slab is mainly stabilized by slab lattice polarization instead of surface electronic compensation, with minor contribution from surface metallization, with charge transfer taking place between the two counter terminations [the critical thickness above which $LaAlO_3$ (001) metallizes is 4 to 5 unit cells [54,77]]. In other words, slab lattice polarization accompanied with little surface compensating charge is introduced in the 16-layer asymmetric slab model [Fig. 25(a)], and the built-in electric field (total dipole moment) in the slab leads to the observed band bending between the two surface terminations.

The symmetric slab calculations have excess charge doping from off-stoichiometry available to compensate their polar surfaces in exactly the same way as would be compensated in the high thickness limit. Therefore, lattice polarization does not occur in the $LaAlO_3$ 15-layer symmetric slabs except for the top surface layers. These top layers still exhibit ionic polarization although to a smaller extent than those of the 16-layer asymmetric slab, and the coordinates of atoms below the surface layers are close to the bulk symmetry.

Assuming that the slab thickness is large enough so that the surface compensating charge screens the dipole within half the cell and there is a bulklike region in the slab, one would expect that there is no interaction (or charge transfer) between the two counter surfaces for the asymmetric slab. From the electrostatic potential profiles shown in Fig. 3(a), it is clear that the two surfaces of the 16-layer $LaAlO_3$ asymmetric slab are still interacting with each other, suggesting there is no bulklike region in the $LaAlO_3$ asymmetric slab. The nonconverged surface properties of the $LaAlO_3$ 16-layer (001) slab models are also supported by the $LaAlO_3$ surface energy results below in Sec. III D, where the surface energy of an asymmetric slab is still much lower than those averaged from the two symmetric slabs.

The E_{Fermi}s of the15-layer AO and BO_2 symmetric models are both pinned by the surface states with almost no band bending observed in the DOS plots [see the electrostatic potential profiles in Fig. 3(a) as well as the slab band structure in Fig. 4 below, i.e., almost no spreading of band structures in Figs. 4(b) and 4(c) vs dispersed band structure in Fig. 4(a)] between the surface and the central layer of the slab. Therefore, all the discussed results above suggest screening of the dipole for the perfect $LaAlO_3$ (001) surfaces, requiring a large number of layers, and consequently the simulated slabs in this paper (thickness up to 15 or 16 layers) do not contain a bulklike region.

2. *Weakly polarized $SrTiO_3$ (001) surfaces*

Figure 5 shows the DOS plots of $SrTiO_3$ (001) asymmetric/stoichiometric 16-layer slab and symmetric BO_2 as well as AO terminated 15-layer slabs, compared to the bulk DOS

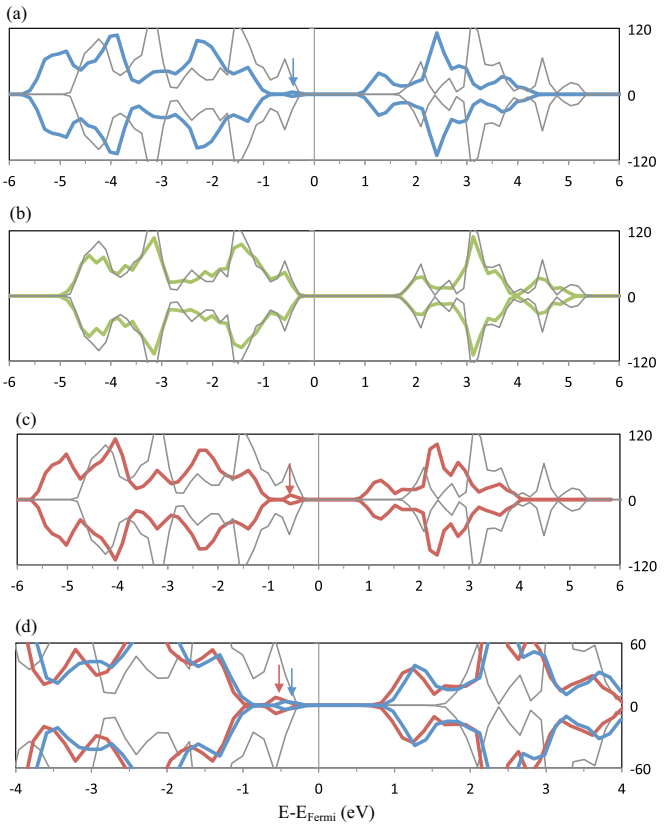

FIG. 5. (Color online) Plots of calculated DOS for $SrTiO_3$ (a) asymmetric 16-layer (001) slab, (b) symmetric 15-layer-SrO-terminated (001) slab, and (c) symmetric 15-layer-TiO_2-terminated (001) slab. Plot (d) is a zoom-in and overlapped DOS between the asymmetric 16-layer slab [i.e., plot (a)] and the symmetric 15-layer-TiO_2-terminated slab [i.e., plot (c)]. In each plot, thick and thin solid lines represent the slab and the bulk DOS, respectively. The Fermi energy level is aligned at 0, and the arrows indicate the TiO_2 surface states. The slight downshift of the whole band structure for the symmetric 15-layer-TiO_2-terminated slab relative to the asymmetric 16-layer slab shown in plot (d) suggests the different surface Fermi level pinning or surface band bending between the two slab models.

(represented with a thin gray line in each plot). As addressed previously in Sec. III A, bond breaking compensates for the weakly polar $SrTiO_3$ (001) surfaces so that the band structure of $SrTiO_3$ is only slightly modified with respect to its bulk. Nonetheless, a ~0.5 eV downshift of the entire slab band structure relative to the Fermi energy as compared to the bulk can be observed in both the DOS plots of 16-layer asymmetric slab [Fig. 5(a)] and 15-layer BO_2 (or TiO_2) terminated slab [Fig. 5(c)], while the 15-layer SrO terminated slab exhibits very similar band structure with no energy shift [Fig. 5(b)]. Such downshift of the whole band structure in Figs. 5(a) and 5(c) is caused by the existence of surface states from less hybridized surface O $2p$ orbitals with Ti $3d$ states [52]. In other words, if we align the core level band structures of the slab models containing TiO_2 surfaces with the bulk, the existence of the TiO_2 surface states, in fact, shifts up the Fermi level, which suggests an increase of electron chemical potential of the whole slab relative to the bulk. In addition, Fig. 5(d) shows that the 15-layer TiO_2 symmetric slab has

a slightly higher Fermi level than the 16-layer asymmetric slab, consistent with the surface layer charge results shown in Fig. 25(b) of the Appendix, which was ascribed to electronic redistribution between the two counter surface terminations of the 16-layer $SrTiO_3$ asymmetric slab. As will be shown below, such an increase in electron chemical potential of the slab due to the existence of the TiO_2 surface states and electronic redistribution between the two surfaces of the asymmetric slab leads to slight differences in the surface energy averaged between the two symmetric slabs vs that of the asymmetric slab (Sec. III D) and further leads to the stabilization of cation vacancies relative to the bulk across the whole slabs as well as dissimilar surface cation vacancy energies among the three $SrTiO_3$ slab models in this paper (%Sec. IV B 2).

3. *Polar $LaMnO_3$ (001) surfaces*

Figure 6 shows the DOS plots of the $LaMnO_3$ (001) asymmetric 16-layer slab and the symmetric BO_2 and AO terminated 15-layer slabs, as compared to the bulk DOS (represented with a thin gray line in each plot). It is seen that the DOS plots of the three slab models all resemble their bulk, except for a slight shift of the whole band and broadening of the peaks (become wider and smoother than the bulk). The broadening of the peaks is due to a superposition of the projected layer band structures with a slight shift in energy level (i.e., surface band bending), due to the introduced surface compensating charge. The introduction of additional surface compensating charge produces local electric field near the surface terminations but removes the macroscopic electric field caused by the layer charge dipole of the 16-layer stoichiometric slab. The almost identical band structures of stoichiometric

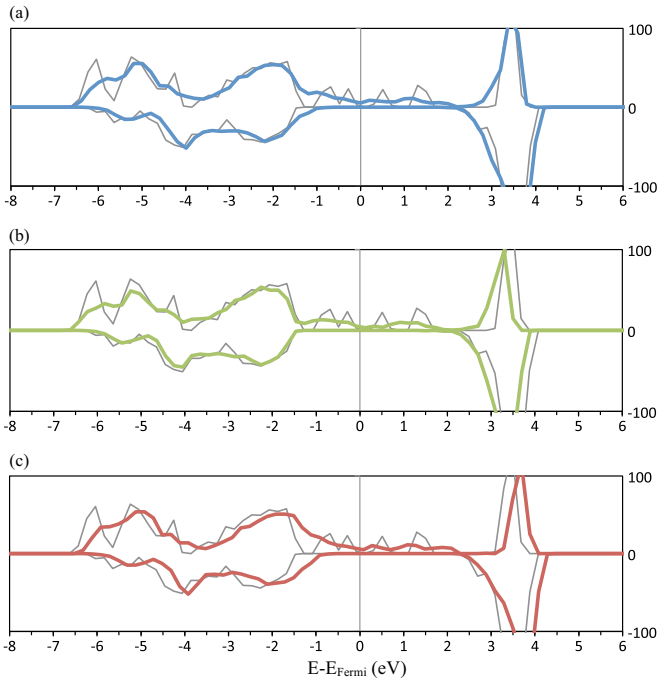

FIG. 6. (Color online) Plots of calculated DOS for $LaMnO_3$ (a) asymmetric 16-layer-slab, (b) symmetric 15-layer-AO-terminated slab, and (c) symmetric 15-layer-BO_2-terminated slab. In each plot, thick and thin solid lines represent the slab and the bulk DOS, respectively, and the Fermi energy level is aligned at 0.

bilayers (adjacent $AO + BO_2$ layers) between the 16-layer stoichiometric slab and 15-layer symmetric slabs shown in Fig. 7 suggest that the two slab model surfaces are essentially identical, which supports that the surface compensating charge is effectively screened in both $LaMnO_3$ slabs. That the 15-layer slab surface band structures are found to be the same as those of the 16-layer surfaces is consistent with the surface energy results shown in Sec. III D, where the surface energies of the 15-layer and 16-layer slab models are almost identical.

D. Surface energy of perfect $LaAlO_3$, $SrTiO_3$, and $LaMnO_3$ (001) surfaces

Figure 8 shows calculated surface energies (with both symmetric and asymmetric slab models) vs slab thickness for $LaAlO_3$, $SrTiO_3$, and $LaMnO_3$. The surface energies are derived via the following equations:

$$\Delta E^{surf}_{asym} = \frac{1}{2}\left(E_{asym\_slab}(N) - \frac{N}{4} \bullet E_{2\times2\times2\_bulk}\right), \quad (N = 4,8, \text{ and } 16) \tag{2}$$

$$\Delta E^{surf}_{sym} = \frac{1}{4}\left(E_{AO\_slab}(N) + E_{BO_2\_slab}(N) - \frac{N}{2} \bullet E_{2\times2\times2\_bulk}\right), \quad (N = 5,9, \text{ and } 15), \tag{3}$$

where ΔE^{surf}_{asym} and ΔE^{surf}_{sym} are the calculated surface energies of the asymmetric and symmetric slabs, respectively, and $E_{asym\_slab}(N)$, $E_{AO\_slab}(N)$, $E_{BO_2\_slab}(N)$, and $E_{2\times2\times2\_bulk}$ are the calculated total energies of N-layer asymmetric slab ($N = 4, 8, 16$), N-layer AO terminated symmetric slab ($N = 5, 9, 15$), N-layer BO_2 terminated symmetric slab ($N = 5, 9, 15$), and $2 \times 2 \times 2$ bulk, respectively. Both ΔE^{surf}_{asym} and ΔE^{surf}_{sym} represent the averaged surface energy of the AO and BO_2 surface for the asymmetric and symmetric slab models. While one could estimate the AO or the BO_2 surface energy separately in the symmetric slab models at given metal and oxygen chemical potential references [74], a direct comparison of surface energies among the three systems based on such method is inaccessible, since there is no unique choice of metal chemical potential reference determined at a specified oxygen chemical potential for comparison among the $LaMnO_3$, $SrTiO_3$, and $LaAlO_3$ systems. Therefore, when we refer to surface energy below we will always mean it to be the average surface energy, which allows us to use the bulk energy as the reference and make direct comparison of surface energy between the symmetric and asymmetric slab models among the three materials systems.

In Fig. 8, the surface energy of symmetric slabs does not show significant thickness dependence for any of the three systems in this paper. For the strong polar systems, the symmetric slab calculations contain excess surface charge doping in exactly the same way as the polar surfaces would be compensated in the high thickness limit. Therefore, the thickness independent surface energy mainly reflects on the enforced charge doping by the off-stoichiometry of the slab models. Interestingly, although the $LaMnO_3$ (001) and $LaAlO_3$

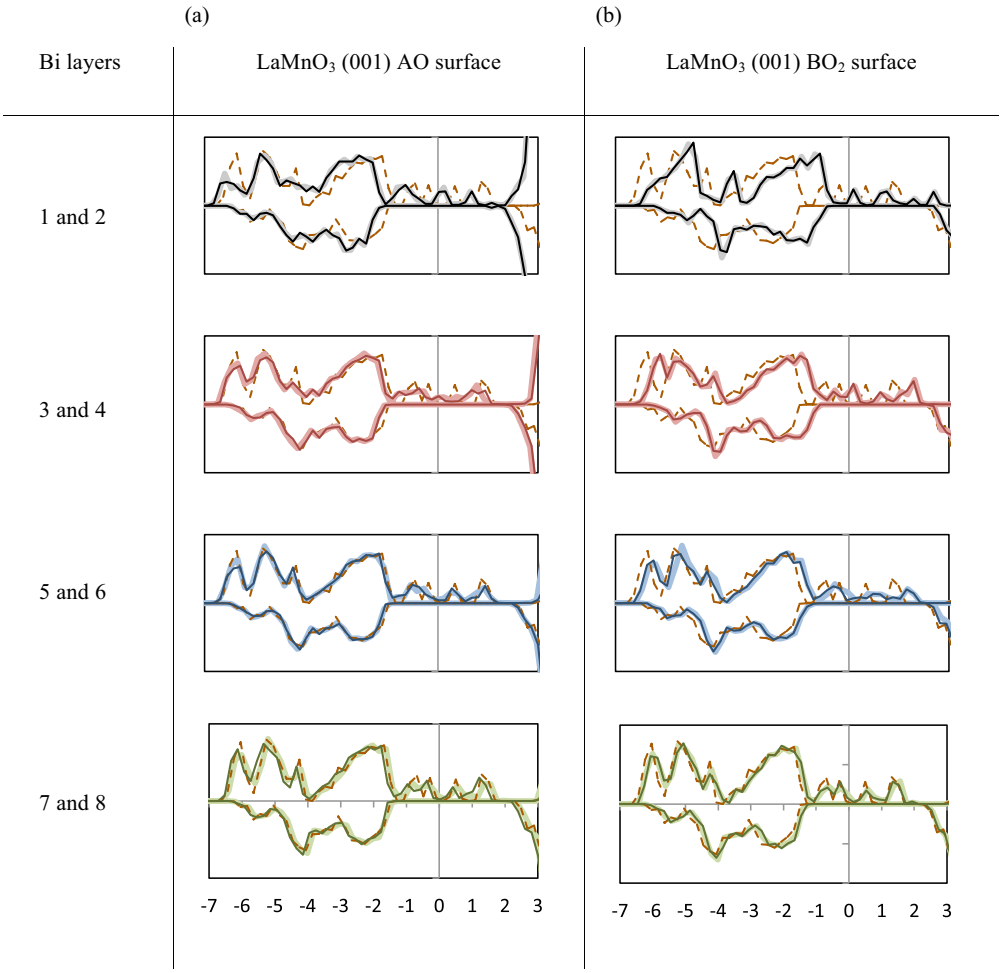

FIG. 7. (Color online) Plots of calculated projected DOS for stoichiometric bi-layers (two adjacent AO and BO_2 layers) of $LaMnO_3$ (a) (001) AO surfaces and (b) (001) BO_2 surfaces. In each plot, thick (lighter) and thin (darker) lines are the projected stoichiometric layer DOS of the 16-layer asymmetric slab and the 15-layer symmetric slab, respectively, and a dashed line represents the normalized bulk DOS. The Fermi energy level is aligned at 0.

surfaces are much more polar than the $SrTiO_3$ (001) surface, the difference in energy between $LaMnO_3$ and STO is only

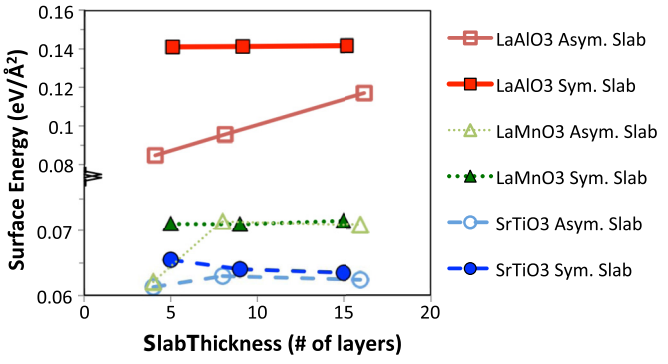

FIG. 8. (Color online) Calculated surface energy of the (001) slabs vs slab thickness for $LaAlO_3$ (red squares), $SrTiO_3$ (green triangles), and $LaMnO_3$ (blue circles). Data of asymmetric slabs and symmetric slabs are plotted with solid and empty symbols, respectively. The lines connecting the data shown in the plot are guides to the eye. Note that the ordinate axis scale changes at 0.8 to enable more complete visualization of the data.

$\sim 0.01\,eV/Å^2$ ($0.16 J/m^2$) but is as large as $\sim 0.08\,eV/Å^2$ ($1.28\,J/m^2$) between $LaAlO_3$ and $SrTiO_3$. The similarity of $LaMnO_3$ to $SrTiO_3$ and the large difference of $LaAlO_3$ compared to $SrTiO_3$ likely reflects the lower energy cost for electron redistribution at mixed ionic-electronic conducting oxide polar surfaces ($LaMnO_3$/LSM) compared to polar surfaces of a wide band gap insulator (e.g., $LaAlO_3$).

Although the order of surface stability relative to the bulk for the three systems remains the same using the asymmetric slab model, the surface energies of $LaAlO_3$ and $LaMnO_3$ (001) polar surfaces exhibit strong thickness dependence due to the fact that the total dipole moment or the built-in electric field potential in the slab grows with N. Interestingly it is seen in Fig. 8 that the $LaMnO_3$ (001) asymmetric slab surface energy converges to that of symmetric slabs at just ~ 8 layers. This $LaMnO_3$ behavior is in contrast to the $LaAlO_3$ (001) surfaces, which would require a very thick slab model to see the convergence of the asymmetric slab surface energy to the infinite thickness limit [the extrapolated intercept of the (001) surface energy vs thickness lines between the $LaAlO_3$ asymmetric and symmetric slab models shown in Fig. 8 is located at thickness ~ 26 layers]. Also, in the low thickness

regime (<8 layers), surface energy of the $LaMnO_3$ (001) asymmetric four-layer slab is close to that of the $SrTiO_3$ (001) four-layer slab, suggesting that when the total dipole moment is reduced by decreasing the slab thickness, $LaMnO_3$ (001) could have comparable or even smaller surface energy than $SrTiO_3$ (001).

Unlike $LaAlO_3$ and $LaMnO_3$, the weak polar (or nonpolar in terms of the formal charge) $SrTiO_3$ surface energy exhibits no clear thickness dependence for the asymmetric slabs and is lower than the other two strong polar systems. This result can be understood by the fact that the weak polarity of $SrTiO_3$ (originated from covalency between the metal-oxygen bond) does not require introducing additional surface compensating charge. Despite the lower (001) surface energy for $SrTiO_3$ than $LaMnO_3$, a small energy difference exists between the surface energies of $SrTiO_3$ symmetric and asymmetric (001) slabs, which is due to different E_{Fermi} pinning (vs aligned band features such as O $2p$ band) by the TiO_2 surface states among the simulated slab models. The variation of the E_{Fermi}s among the slab models suggests that although $SrTiO_3$ contains a TM and is not a strong polar system, the Ti $3d^0$ character with a charge transfer gap (the GGA gap in this paper is 1.5 eV between the occupied O $2p$ band and the unoccupied Ti $3d$ band) still leads to nonconverged surface energy between the asymmetric and symmetric slab models. While in surface energy results, the TiO_2 surface states only cause a slight energy difference, more significant influence appears in the cation vacancy formation energies, which will be discussed in %Sec. IV B 2.C below.

IV. SURFACE DEFECT ENERGETICS

In this section we discuss the surface defect energies and how they couple to properties of each surface and compound. We first summarize the charge nature of the point defects and the polar surfaces as a guide for understanding their electrostatic interactions in Sec. IV A. Then the overall surface defect energetic results are categorized into two point defect types based on the nature of the point defect charge [i.e., oxygen vacancies vs cation vacancies and Sr'_A doping for the two (001) AO and BO_2 surface terminations in the two slab models—the 15-layer symmetric and 16-layer asymmetric slabs], which consists of a total of eight cases for each material system. In Sec. IV B, the surface defect energetics results of each material system are discussed by a general pattern that we first focus on oxygen vacancies and compare the surface defect energetics for the two types of surface terminations in two different slab models. We then move on to discussions for cation vacancies/Sr'_A doping. Additional notes or results that are specific to a material system may be added at the end of discussions.

A. Charge of point defects and (001) surfaces

Table II summarizes formal charge and charge doping for cation and anion point defects (here we focus on vacancies as interstitials are generally not energetically favorable to form in the close packed perovskite systems) and (001) AO and BO_2 surfaces for $LaAlO_3$, $SrTiO_3$, and $LaMnO_3$, based on the fully ionic limit. The charge doping for defects represents the electrons or holes that used to reside on an atom and which are returned to the material by creation of the defect. The charge doping for surfaces represents the compensating charge needed at the polar surfaces to avoid electrostatic divergence according to Tasker's criteria [79]. We note that covalency effects between metal and oxygen bonding may influence the magnitude of charge doping for point defects and surface compensating charge for strong polar (001) surfaces and also cause weak polarity for $SrTiO_3$ (001) surfaces [32]. Nonetheless, the fully ionic limit provides guidance of how point defects are likely to interact with the polar surfaces

TABLE II. Formal charge and charge doping of point defects and (001) AO and BO_2 surfaces (defined as the surface layer charge relative to the bulk layer) for $LaAlO_3$, $SrTiO_3$, and $LaMnO_3$ based on the scenario of the fully ionic limit.

	Point defects			Electronically compensated (001) AO surfaces		Electronically compensated (001) BO_2 surfaces	
	Defect type	Formal charge (per defect)	Charge Doping per defect)	Formal charge ($\sigma^{\text{surf}} = 1/2 \bullet \sigma^{\text{bulk}}$, per perovskite unit cell area)	Charge Doping[a] (per perovskite unit cell area)	Formal charge ($\sigma^{\text{surf}} = 1/2 \bullet \sigma^{\text{bulk}}$, per perovskite unit cell area)	Charge Doping[a] (per perovskite unit cell area)
$LaAlO_3$	$[V\ddot{o}]$	+2	–2	+0.5	–0.5	–0.5	+0.5
	$[V'''_A]$	–3	+3				
	$[V'''_B]$	–3	+3				
$SrTiO_3$	$[V\ddot{o}]$	+2	–2	0	0	0	0
	$[V''_A]$	–2	+2				
	$[V''''_B]$	–4	+4				
$LaMnO_3$	$[V\ddot{o}]$	+2	–2	+0.5	–0.5	–0.5	+0.5
	$[V'''_A]$	–3	+3				
	$[V'''_B]$	–3	+3				
	$[Sr'_A]$	–1	+1				

[a]The surface charge doping (ΔQ) is derived based on the $\Delta Q = \sigma^{\text{surf}} - \sigma^{\text{bulk}}$, where σ^{surf} and σ^{bulk} are the surface and bulk layer charge, respectively. For polar (001) surfaces, polarity requires $\sigma^{\text{surf}} = 1/2 \bullet \sigma^{\text{bulk}}$ to eliminate divergence of the electrostatic energy at high thickness limit [32,79]. Therefore, in the fully ionic limit, the (001) polar surfaces will have surface charge doping equal to $\sigma^{\text{surf}} - \sigma^{\text{bulk}} = -1/2 \bullet \sigma^{\text{bulk}}$.

based on the positive or negative nature of the introduced charge doping. For example, both $V\ddot{o}$ and strong polar (001) AO surfaces are positively charged (or both contain negative charge doping), and their interaction can be considered as repulsive, while attractive interaction is expected between $V\ddot{o}$ and strong polar (001) BO surfaces.

B. Defect *E*s of perovskite (001) surfaces

1. *Defect Es of perfect $LaAlO_3$ (001) strong polar surfaces*

(a) Defect Es of $LaAlO_3$ bulk. Due to the large band gap in $LaAlO_3$, the bulk point defect energetics are strongly influenced by the electron chemical potential or Fermi level of $LaAlO_3$. An *ab initio*-based study for $LaAlO_3$ bulk defect energetics vs Fermi level has been investigated by Luo *et al.* [72], where bulk point defect formation energies can vary by 5–15 eV depending on the Fermi level of the $LaAlO_3$ bulk and the defect charge states. Since only one defect charge state (i.e., defect calculations without manually adding/removing background charge in the DFT models) is considered in this paper, and the introduced point defect concentration based on the finite size supercell models is significantly higher than the dilute limit, the defined bulk references for calculating E_{seg}s for $LaAlO_3$ in the discussions below are mainly for comparison among the three investigated perovskite systems and should not be taken as a guide for bulk defect formation energies in $LaAlO_3$. We note that by altering the Fermi level of the $LaAlO_3$ bulk surface band bending will also be adjusted, leading to a change in the surface energy and surface point defect formation energies. Therefore, significant further work beyond the scope of this paper is required to properly treat point defects at different charge states in the bulk and slab models [80].

(b) Oxygen vacancy segregation energy of perfect $LaAlO_3$ (001) polar surfaces. Figure 9 shows the calculated O vacancy segregation energies $[E_{seg}(V\ddot{o})]$ for the top eight layers of $LaAlO_3$ (001) slabs, including both 15-layer symmetric and 16-layer asymmetric slab models. For the 15-layer BO_2 terminated slab (filled blue circles in Fig. 9), the $V\ddot{o}$ is the most stable at the top BO_2 terminated surface (stabilized by $\sim$6 eV relative to the bulk) and is gradually destabilized in going from the top surface layer to the central plane, where the $E_{seg}(V\ddot{o})$ is still -4.3 eV more stable as compared to the bulk. The large stabilization of O vacancy ($-4.3\sim-6$ eV) in the BO_2 terminated slab is due to intrinsic hole doping in the 15-layer symmetric $LaAlO_3$ slab model, as previously shown in Fig. 4(c). Formation of $V\ddot{o}$ liberates two electrons, and in the bulk system these electrons fill defect states in the gap close to the conduction band minimum (CBM) [81], while in the hole-doped $LaAlO_3$ symmetric slab these electrons can fill levels near the valence band maximum (VBM), which costs significantly less energy than filling near the CBM. Again, the fact that $E_{seg}(V\ddot{o})$ in the center layer of the 15-layer slab does not converge to the bulk (i.e., yield a zero segregation energy) is consistent with the fact that the surface charge screening length is much longer than the thickness of the simulated symmetric slab for $LaAlO_3$.

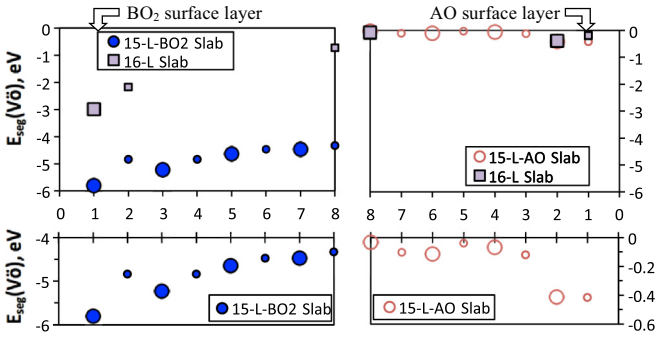

FIG. 9. (Color online) O vacancy segregation energies, $E_{seg}(V\ddot{o}) = E_{surf}(V\ddot{o}) - E_{bulk}(V\ddot{o})$, for the top eight layers of $LaAlO_3$ (001) slabs: filled blue circles represent the data of a 15-layer BO_2 terminated slab (two BO_2 surfaces), empty red circles represent the data of a 15-layer AO terminated slab (two AO surfaces), and filled purple squares represent the data of a 16-layer stoichiometric slab (with one AO and one BO_2 surfaces). The subplots at the bottom are rescaled from the plots above to illustrate the surface effect in $E_{seg}(V\ddot{o})$ from the top layer to the middle layer of the slab. The use of larger and smaller symbols is to highlight the dissimilar trends of the $E_{seg}(V\ddot{o})$s in the AO and BO_2 layers, respectively.

In the case of electron doped $LaAlO_3$ (001) symmetric AO slab, the E_{Fermi} is pinned by the AO surface states and is close to the CBM, as shown previously in Fig. 4(b). While the energy of $V\ddot{o}$ formation in mixed ionic-electronic conductors can often be described by two electrons going from the O $2p$ band center to E_{Fermi} [6], the energy levels of the $V\ddot{o}$ defect states localized around the O vacancy in the metallized AO surface are lower in energy than the AO surface states [81]. The energy of the electrons involved in this defect formation is quite similar to the case of the bulk vacancy formation, where two electrons move from the O $2p$ band to the defect states close to the CBM. Therefore, both the AO terminated slab and the bulk exhibit comparable O vacancy formation energy in this paper. The small stabilization of O vacancy formation (~-0.4 eV) relative to the bulk for the top surface layer of the AO terminated slab may be attributed to breaking fewer or weaker metal-oxygen bonds at the surface layer than in the bulk in forming an O vacancy. Note that although the formation of a subsurface BO_2 layer O vacancy has the same number of bonds breaking as in the bulk, it involves the breaking of four bonds between a subsurface layer O and four undercoordinated top surface layer La atoms, which have La-O bonds that are weaker than the La-O bonding in the bulk due to extra electrons (from surface polarity compensation) filling in the antibonding states.

For the 16-layer stoichiometric slab, Fig. 9 shows that there is much less stabilization of $V\ddot{o}$ at the BO_2 surface layer [$E_{seg}(V\ddot{o})$ is about 3 eV higher] as compared to that of the 15-layer BO_2 terminated slab. We propose that this reduction is due to the large positive compensating charge introduced by off-stoichiometry in the 15-layer slab, whose charge does not occur in the 16-layer asymmetric slab. The $V\ddot{o}$ is generally destabilized due to it donating negative charges to high-energy states; therefore, the presence of excess positive charge can stabilize the $V\ddot{o}$ significantly.

(c) Cation vacancy segregation energy of perfect $LaAlO_3$ (001) polar surfaces. Figure 10 shows the calculated cation vacancy segregation energies $[E_{seg}(V_A'''/V_B''')]$ for the top

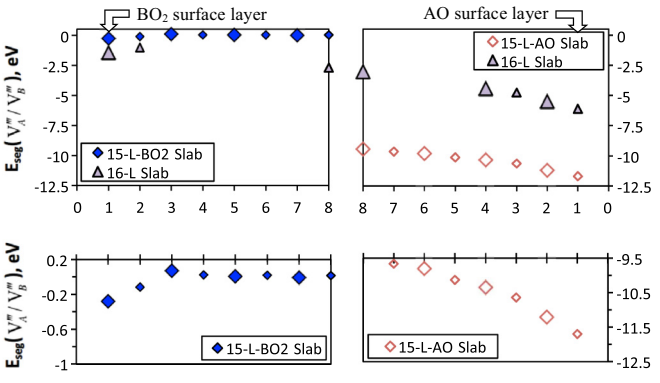

FIG. 10. (Color online) Cation vacancy segregation energies, $E_{seg}(V_A'''/V_B''')$, for the top eight layers of $LaAlO_3$ (001) slabs: filled blue diamonds represent the data of a 15-layer BO_2 terminated slab (two BO_2 surfaces), empty red diamonds represent the data of a 15-layer AO terminated slab (two AO surfaces), and filled purple triangles represent the data of a 16-layer stoichiometric slab (with the BO_2 surface on the left and the AO surface on the right). The subplots at the bottom are rescaled from the plots above to illustrate the surface effect in $E_{seg}(V_A'''/V_B''')$ from the top layer to the middle layer of the slab. The larger and smaller symbols represent B-site cation vacancy and A-site cation vacancy segregation energies, respectively.

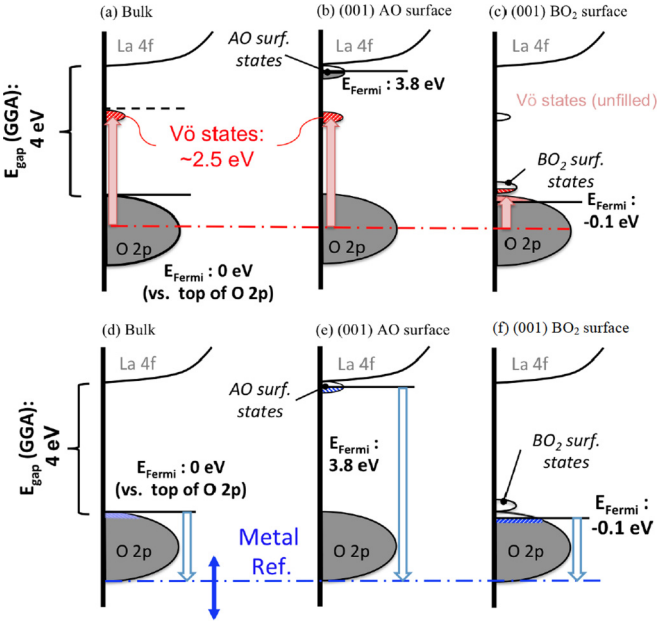

FIG. 11. (Color online) Energy level diagram for electron transfer in formation of (a) bulk $Vö$, (b) (001) AO surface $Vö$, (c) (001) BO_2 surface $Vö$, (d) bulk V_A'''/V_B''', (e) (001) AO surface V_A'''/V_B''', and (f) (001) BO_2 surface V_A'''/V_B''' for the $LaAlO_3$ bulk and (001) AO and BO_2 surfaces of the symmetric slab models. All energy is referenced to the top of the O $2p$ band, including Fermi level of the bulk and surfaces. The dashed line in (a) for $Vö$ formation in the bulk $LaAlO_3$ represents the Fermi level of the bulk supercell containing $Vö$. The red and blue dash-dotted lines indicate the O $2p$ band center and the metal references of $LaAlO_3$, respectively. The metal references are not uniquely defined in perovskites (see discussions in Sec. II), and their range is indicated by the blue double arrow (only for guiding without quantitative meaning). The schematic plots shown here do not include band structure change due to surface relaxation and bond breaking.

eight layers of $LaAlO_3$ (001) slabs, including both 15-layer symmetric and 16-layer asymmetric slab models. It is seen that the $E_{seg}(V_A'''/V_B''')$ trends are similar to the case of $E_{seg}(Vö)$ but now they go in the opposite direction, and the magnitude of $E_{seg}(V_A'''/V_B''')$s are larger than that of $E_{seg}(Vö)$s. The change in sign and increased magnitude of $E_{seg}(V_A'''/V_B''')$s compared to $E_{seg}(Vö)$s can be understood in terms of the change in sign and increased magnitude of the defect charge on compared to $Vö$ defects.

(d) The influence of the $LaAlO_3$ band gap, defect states, and surface states on surface defect Es. When the defects have the same charge doping as the $LaAlO_3$ polar surface to which they are segregating, it is seen that point defects have almost zero segregation energies. For example, $E_{seg}(V_A'''/V_B''')$s near the BO_2 termination (both have positive charge doping) of the 16-layer (001) slab are almost the same as those of the 15-layer BO_2 slab and are quite close to zero [i.e., the defect energy near the surface is close to that in the bulk (see Fig. 10)]. A similar result is observed previously for $E_{seg}(Vö)$s near the AO termination (both have negative charge doping) of the 16-layer slab and the 15-layer AO symmetric slab (Fig. 9). That the surface defect energetics for point defects with the same charge doping type as that of polar surfaces are much closer to the bulk defect energetics than those at the counter surfaces can be explained by surface Fermi level pinning and localization of defect states due to the large band gap of $LaAlO_3$. In Fig. 11, we show the energy level diagrams for electron transfer in formation of $Vö$ and V_A'''/V_B''' between the bulk $LaAlO_3$ and the (001) surfaces. To reflect on the Fermi level pinning by the existence of the (001) AO and BO_2 surface states, all energies shown in Fig. 11 are referenced to the top of the O $2p$ band. It is seen that when point defects contain the same charge type as the polar surfaces, the energy for the electron interchange in formation of $Vö$ and V_A'''/V_B''' is very close to that of the bulk. On the other hand, formation of point defects with the counter charge to the strong polar surfaces accommodates surface charge by filling the surface hole states near VBM in the case of $Vö$ at the BO_2 surfaces or removing the AO surface electron states near CBM for V_A'''/V_B''' at the AO surfaces, which leads to significant stabilization of the surface point defects relative to the bulk. In addition, it is seen that the top surface layer $E_{seg}(Vö)$ of the 15-layer BO_2 symmetric slab (−5.8 eV, Fig. 10) is close to twice the energy level difference between the BO_2 surface state (−0.1 eV relative to the top of the O $2p$ band) and the bulk $Vö$ defect state (+2.5 eV vs the top of the O $2p$ band). Similarly, the top surface layer $E_{seg}(V_A'''/V_B''')$s of the 15-layer AO symmetric slab −11.7 eV (Fig. 9) is close to triple the energy level difference between the Fermi level of the AO surfaces (+3.8 eV) and the Fermi level of the bulk (0 eV relative to the top of the O $2p$ band). Therefore, our results suggest energy level differences in electron exchange in formation of point defects between surfaces and bulk are the main driving force for the observed surface $E_{seg}(Vö)$ and $E_{seg}(V_A'''/V_B''')$s shown in Fig. 9 and Fig. 10 (with relatively small contributions at the scale of a few hundred meV from other factors, e.g., surface strain relaxation and bond breaking).

2. *Defect Es of perfect $SrTiO_3$ (001) weakly polar surfaces*

(a) Defect Es of $SrTiO_3$ bulk. The ideal $SrTiO_3$ (001) surfaces contain weak polarity, and no additional surface charge is needed for compensating the dipole divergence as seen in the case of the strong polar surfaces. However, similar to $LaAlO_3$, $SrTiO_3$ also contains a band gap due to the Ti (d^0) configuration. An *ab initio* based study for $SrTiO_3$ bulk defect energetics vs Fermi level has been investigated by Tanaka *et al.* [73], where bulk point defect formation energies can vary by 5–15 eV depending on the Fermi level of the $SrTiO_3$ bulk and the defect charge states. Similar to the $LaAlO_3$ system, we note that the defined bulk references for the E_{seg}s of $SrTiO_3$ (001) surfaces in the discussions below are mainly for comparison with the $LaMnO_3$ system, and further work would be needed to include different charge states for the point defects, to obtain correct band gap and defect energy levels, to consistently bridge the surfaces with the bulk through the electron chemical potentials or Fermi level, and to properly treat spurious electrostatic interaction in the finite size periodic supercells [80].

(b) Oxygen vacancy segregation energy. Figure 12 shows the calculated $E_{seg}(V\ddot{o})$s for top eight layers of $SrTiO_3$ (001) 15-layer symmetric and 16-layer asymmetric slabs. Carrasco *et al.* [53] reported that the $SrTiO_3$ (001) TiO_2 surface $E_{seg}(V\ddot{o})$s is about 1.5 eV, which is 0.7 eV lower than the value in this paper. The difference comes from the supercell size dependence in calculating the bulk and slab O vacancy formation energies (spurious electrostatic interaction in the supercell with different dimensions), which we have made a particular effort to cancel effectively in this paper.

The $E_{seg}(V\ddot{o})$s are much closer to the $SrTiO_3$ bulk reference value (within -1.0–0.6 eV) as compared to those of the $LaAlO_3$ (001) polar surfaces. Such difference between the trends of $LaAlO_3$ and $SrTiO_3$ surface $E_{seg}(V\ddot{o})$s is due to the fact that the $SrTiO_3$ (001) surface electronic structures remains close to its bulk since surface bond breaking allows $SrTiO_3$ surfaces to compensate their weak polarity [32] and no metallization occurs for the $SrTiO_3$ (001) surfaces (as shown in Fig. 5). It is noticed that although E_{Fermi} of the SrO 15-layer symmetric slab (no TiO_2 surface states in the gap) is lower than those of 15-layer TiO_2 symmetric and the 16-layer stoichiometric slab (the TiO_2 surface states shifts up the E_{Fermi}s), the E_{Fermi} difference does not affect electron interchange between the O $2p$ band and the $V\ddot{o}$ defect states [6]. Therefore, the $E_{seg}(V\ddot{o})$s of both the $SrTiO_3$ (001) symmetric and asymmetric slab models are found to be almost identical since $E_{seg}(V\ddot{o})$s are governed by filling of the defect states at the energy level of close to the CBM relative to the occupied O $2p$ states, regardless of the E_{Fermi} difference caused by the presence of the (001) TiO_2 surface states.

The oscillation of the $E_{seg}(V\ddot{o})$s near the $SrTiO_3$ (001) surface terminations is likely to be caused by the finite size along in-plane [orthogonal to the (001) surface] directions of the periodic slab simulations. In this paper, our slab models contain a 2×2 cross-section, and creating a $V\ddot{o}$ (in-plane concentration $= 1/4$ for $V\ddot{o}$ in the AO plane and $= 1/8$ for $V\ddot{o}$ in the BO_2 plane) leads to a strong perturbation in the weakly polar $SrTiO_3$ (001) slabs, which would cause a change in the in-plane layer charge and hence influence the slab energy through change of the total electrostatic field.

Note that for the top surface layer, reduced bonding of surface atoms (coordination) and relaxation of strain near point defects on the surfaces vs the bulk also contributes to surface defect segregation energies. Both coordination effect and surface strain relaxation are expected to stabilize cation and oxygen vacancies at surfaces vs the bulk since surface atoms contain less bond breaking and more relaxation is allowed at the surfaces to accommodate strain induced by the point defects. Overall, our calculated $SrTiO_3$ (001) $E_{seg}(V\ddot{o})$s are within the range of ± 1 eV, which is a relatively small fraction of the overall large bulk O vacancy formation energy (5.5 eV in Table II), suggesting that the amount of surface O vacancies would still be very small (although likely orders of magnitude higher than in the bulk) in the oxygen-rich limit.

(c) Cation vacancy segregation energy. In contrast to the similar $E_{seg}(V\ddot{o})$s, dissimilar results of $E_{seg}(V_A''/V_B'''')$s for the $SrTiO_3$ 15-layer symmetric vs 16-layer asymmetric (001) slab models are revealed in Fig. 13. To understand what causes such a difference, we first examine the $E_{seg}(V_A''/V_B'''')$ of the central region of the three slab models. It is seen that the $E_{seg}(V_A''/V_B'''')$s of the SrO terminated symmetric slab are close to the bulk value, while the $E_{seg}(V_A''/V_B'''')$s of the TiO_2 symmetric slab are about -1.2 to -1.5 eV lower than the bulk, and the $E_{seg}(V_A''/V_B'''')$s of the asymmetric slab model are

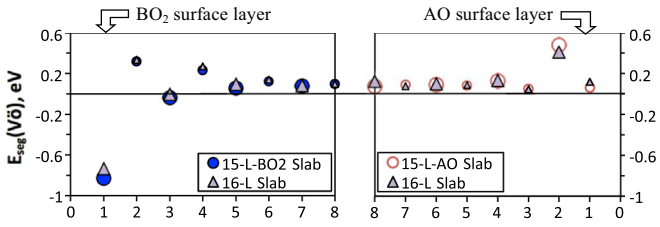

FIG. 12. (Color online) O vacancy segregation energies, $E_{seg}(V\ddot{o})$, for the top eight layers of $SrTiO_3$ (001) slabs: filled blue circles represent the data of a 15-layer BO_2 terminated slab (two BO_2 surfaces), empty red circles represent the data of a 15-layer AO terminated slab (two AO surfaces), and filled purple squares represent the data of a 16-layer stoichiometric slab (one AO and one BO_2 surfaces). The use of larger and smaller symbols highlights the dissimilar trends of the $E_{seg}(V\ddot{o})$s in the AO and BO_2 layers, respectively.

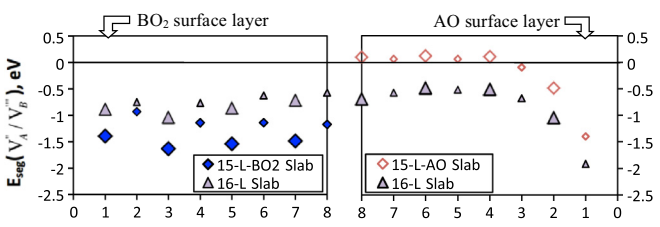

FIG. 13. (Color online) Cation vacancy segregation energies, $E_{seg}(V_A''/V_B'''')$s, for the top eight layers of $SrTiO_3$ (001) slabs: filled blue diamonds represent the data of a 15-layer BO_2 terminated slab (two BO_2 surfaces), empty red diamonds represent the data of a 15-layer AO terminated slab (two AO surfaces), and filled purple triangles represent the data of a 16-layer stoichiometric slab (with the BO_2 surface on the left and the AO surface on the right). The larger and smaller symbols represent B-site cation vacancy and A-site cation vacancy segregation energies, respectively.

between the previous two cases. Considering that a bulklike region in the simulated slab model will have defect energetics the same as the bulk (i.e., defect segregation energy = 0), we conclude that only the SrO terminated symmetric slab contains a bulklike region, while the other two slab models do not. By inspecting Fig. 5 of %Sec. III C 2, it is seen that the main differences among the 15-layer (001) SrO terminated, 15-layer (001) TiO_2 terminated, and 16-layer (001) stoichiometric ($SrO + TiO_2$) slabs are the relative shift of the E_{Fermi} due to the existence/absence of the TiO_2 surface states. The increased stabilization in $E_{seg}(V_A''/V_B'''')$s in the central region of the (001) TiO_2 terminated symmetric slab compared to the SrO terminated symmetric slab suggests that holes created from cation vacancy formation are interacting with the TiO_2 surface states and that such interaction with surface states still persists when creating a cation vacancy in the central region of the TiO_2 symmetric and stoichiometric slabs. In fact, the monotonically lower $E_{seg}(V_A''/V_B'''')$s of the stoichiometric slab compared to the SrO terminated symmetric slab suggests that the TiO_2 surface states even interact with the holes from creating cation vacancies on the SrO side of the asymmetric slab, suggesting that the interacting depth of the TiO_2 surface states with hole doping is larger than the thickness of the slab model. In addition, the even lower $E_{seg}(V_A''/V_B'''')$s of the TiO_2 symmetric slab than those of the stoichiometric slab are consistent with the higher E_{Fermi} of the 15-layer symmetric TiO_2 slab vs the 16-layer asymmetric slab, as shown previously in Fig. 5(d), leading to a further stabilization of the cation vacancies in the symmetric TiO_2 terminated slab. Overall these results demonstrate that even with the weak polarity effect, the surface states can interact significantly with point defects throughout even a quite large unit cell, suggesting the slab models containing the TiO_2 surfaces in this paper do not have a bulklike region.

(d) The influence of the $SrTiO_3$ *band gap, defect states, and surface states on surface defect Es.* In Fig. 14, we show an energy level diagram for electron transfer in formation of $V\ddot{o}$ and V_A''/V_B'''' for the $SrTiO_3$ bulk and (001) AO and BO_2 surfaces. In Figs. 14(a)–14(c), it is seen that the same electron transfer occurs in formation of $V\ddot{o}$ [the electrons are transferred to the $V\ddot{o}$ defect states, despite the E_{Fermi} differences (relative to the band features) between the symmetric and asymmetric slab models]. As a result, there is no clear influence on the $E_{seg}(V\ddot{o})$s between the symmetric and asymmetric slab models (Fig. 12). On the other hand, Figs. 14(d)–14(f) illustrate how the Fermi level differences caused by the TiO_2 surface states and electron redistribution between the SrO and TiO_2 surfaces of the asymmetric slab leads to the observed trends in $E_{seg}(V_A''/V_B'''')$s. Since the (001) SrO symmetric slab model does not contain the TiO_2 surface state, the relative position of band features vs the E_{Fermi} of the slab [Fig. 14(e)] are similar to the bulk [Fig. 14(d)]. This similarity causes the $E_{seg}(V_A''/V_B'''')$s close to the central region of the 15-layer symmetric SrO slab to converge to the bulk values (Fig. 13). The $E_{seg}(V_A''/V_B'''')$s near the SrO termination are still lower than the bulk, which is expected due to surface strain relaxation and reduction of surface charge from surface bond breaking in the formation of cation vacancies. The monotonically lower $E_{seg}(V_A''/V_B'''')$s in the 16-layer asymmetric slab model than those of the 15-layer symmetric SrO slab reflects on the upshift of the E_{Fermi} of

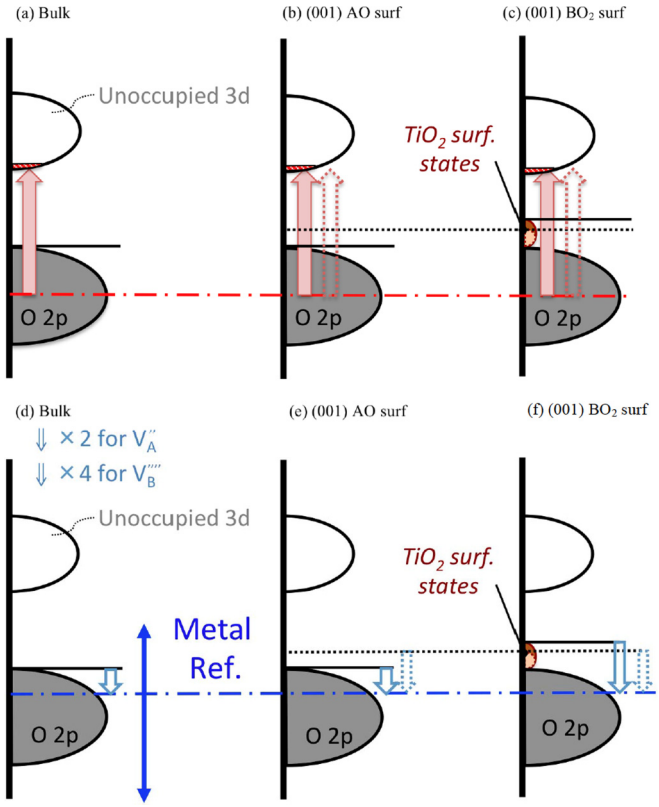

FIG. 14. (Color online) Energy level diagram for electron transfer in formation of (a) bulk $V\ddot{o}$, (b) (001) AO surface $V\ddot{o}$, (c) (001) BO_2 surface $V\ddot{o}$, (d) bulk V_A''/V_B'''', (e) (001) AO surface V_A''/V_B'''', and (f) (001) BO_2 surface V_A''/V_B'''' for the $SrTiO_3$ bulk and (001) AO and BO_2 surfaces. All energy is referenced to the O $2p$ band of the bulk and surface layers. The solid (dotted) horizontal line indicates the Fermi level of the SrO-terminated symmetric (asymmetric) slab model, and the solid (dotted) single arrows represent the energy of electron transfer for defect formation in the SrO-terminated symmetric (asymmetric) slab model. The red and blue dash-dotted lines indicate the O $2p$ band center and the metal references of $SrTiO_3$, respectively. The metal references are not uniquely defined in perovskites (see discussions in Sec. II), and their range is indicated by the blue double arrow (only for guiding without quantitative meaning). The schematic plots shown here do not include band structure change due to surface relaxation and bond breaking.

the 16-layer asymmetric slab caused by the presence of the TiO_2 surface states [dotted lines in Figs. 14(e) and 14(f)], with further adjustment through electron redistribution between the SrO and TiO_2 surfaces. The even lower $E_{seg}(V_A''/V_B'''')$s of the 15-layer symmetric TiO_2 slab than the 16-layer asymmetric slab is due to the fact that the 15-layer symmetric TiO_2 slab contains two TiO_2 surfaces with no electronic redistributions between the two surfaces, which leads to the largest upshift of the E_{Fermi} relative to the band features among the three slab models [Fig. 14(f)]. The origin of the oscillation of $E_{seg}(V_A''/V_B'''')$s in the $SrTiO_3$ slab models is not totally clear at this time but may be attributed to different amount of defect charge between V_A'' and V_B'''' (which is two and four holes, respectively) coupling differently to the surfaces of the slabs.

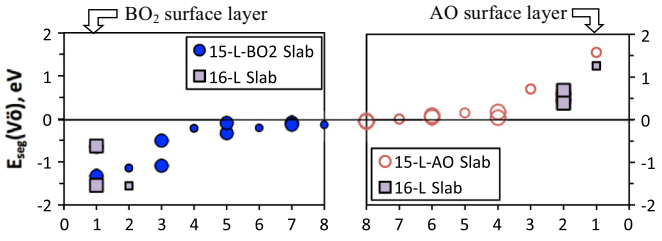

FIG. 15. (Color online) O vacancy segregation energies, $E_{\rm seg}(V\ddot{o})$, for the top eight layers of $LaMnO_3$ (001) slabs: filled blue circles represent the data of a 15-layer BO_2 terminated slab (two BO_2 surfaces), empty red circles represent the data of a 15-layer AO terminated slab (two AO surfaces), and filled purple squares represent the data of a 16-layer stoichiometric slab (one AO and one BO_2 surfaces). The use of larger and smaller symbols highlights the dissimilar trends of the $E_{\rm seg}(V\ddot{o})$s in the AO and BO_2 layers, respectively.

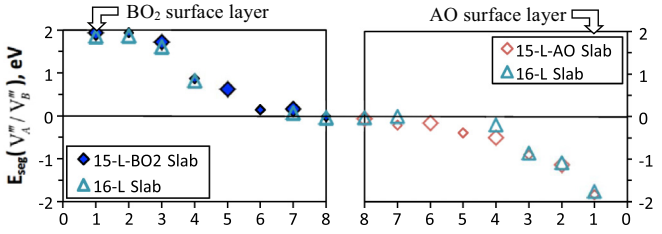

FIG. 16. (Color online) Cation vacancy segregation energies, $E_{\rm seg}(V_A'''/V_B''')$, for the top eight layers of $LaMnO_3$ (001) slabs: filled blue diamonds represent the data of a 15-layer BO_2 terminated slab (two BO_2 surfaces), empty red diamonds represent the data of a 15-layer AO terminated slab (two AO surfaces), and filled purple triangles represent the data of a 16-layer stoichiometric slab (with the BO_2 surface on the left and the AO surface on the right). The larger and smaller symbols represent B-site cation vacancy and A-site cation vacancy segregation energies, respectively.

3. *Defect Es of perfect $LaMnO_3$ (001) polar surfaces*

(a) Defect Es of $LaMnO_3$ bulk. The energetic influence by shifts of the Fermi level (electron chemical potential) from the introduced charge perturbation in the point defect formation is much smaller in the metallic $LaMnO_3$/LSM than systems with large band gaps, since the spurious electrostatic interaction of a point defect in a finite size supercell is effectively screened in $LaMnO_3$/LSM by the more delocalized $3d\,e_g$ electrons and can be effectively described by a defect concentration dependent term [15]. Therefore, more robust bulk defect energetic references for the surface point defect $E_{\rm seg}$s can be obtained with the DFT periodic supercells [15]. As will be illustrated below, the availability of filling and removing TM $3d\,e_g$ electrons near the Fermi level in point defect formation and electronic compensation to the polar surfaces leads to the distinct surface defect properties for $LaMnO_3$/LSM vs $LaAlO_3$ and $SrTiO_3$.

(b) Oxygen vacancy segregation energy. Figure 15 shows the calculated $E_{\rm seg}(V\ddot{o})$s for the top eight layers of $LaMnO_3$ (001) 15-layer symmetric and some partial results of 16-layer asymmetric slabs. The symmetry of $LaMnO_3$ bulk with further symmetry breaking by surfaces results in two distinct $E_{\rm seg}(V\ddot{o})$s at each BO_2 layer near the surface terminations, but they gradually converge to the bulk reference when approaching to the central region of the slabs. The near zero value of $E_{\rm seg}(V\ddot{o})$s near the central region of the slabs and as well as the very similar $E_{\rm seg}(V\ddot{o})$ values for both symmetric and asymmetric slab models suggest that the surfaces of the slabs influence only a nearby region [82], leaving the center of the slab similar to bulk. These results are in agreement with our previous findings: (1) layer-projected DOS plots shown in Fig. 7, where layer projected DOS plots near the central region of both the asymmetric and symmetric slabs are similar to the bulk DOS and the layer-projected DOS plots of 15-layer symmetric vs 16-layer asymmetric slabs can be found to be almost identical; (2) the $LaMnO_3$ (001) surface energies of both asymmetric and symmetric slab models converge to the same value at a small thickness (8 to 9 layers), as shown in Fig. 9; and (3) Bader charge analysis of Fig. 25(c) (in the Appendix) show charges similar to bulk near the middle of the slabs. By all our measures it is found that the metal-like nature of $LaMnO_3$ leads to effective screening of surface dipole, and the screening is short range (∼1.5 nm) and eliminates interactions between the two counter surfaces of the asymmetric slab.

(c) Cation vacancy and Sr segregation energy. In Fig. 16 and Fig. 17, we show that the calculated $E_{\rm seg}(V_A'''/V_B''')$s and $E_{\rm seg}(Sr_A')$s of the $LaMnO_3$ (001) surfaces exhibit similar profiles as moving from surface layers to the center region of the slabs, but the segregation tendency near the two surface terminations is reversed as compared to the $E_{\rm seg}(V\ddot{o})$s. While the magnitude of the defect segregation energies seem to vary among the three defects ($V\ddot{o}$, V_A'''/V_B''', and Sr_A' doping) in the $LaMnO_3$ (001) slab models, after normalizing the defect segregation energies with respect to the formal defect charge doping (i.e., $+3$ for V_A'''/V_B''', $+1$ for Sr_A', and -2 for $V\ddot{o}$), it is seen that the profiles of defect segregation energies vs location of the slab almost fall on top of each other, as shown in Fig. 18. The overlapping of charge normalized surface defect segregation energy vs location profile for the $LaMnO_3$ (001) slabs indicates that defect energetics of unreconstructed $LaMnO_3$ (001) surfaces are mainly governed by interaction between the charge doping introduced from formation of point defects and the charge doping introduced by the surface polarity through changing $3d\,e_g$ electron filling of the TM metal (oxidation states of TM). In Fig. 19, we show an energy

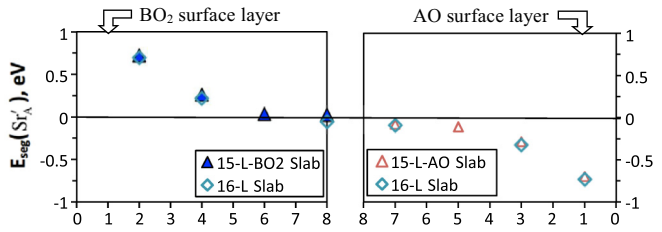

FIG. 17. (Color online) Sr_A' segregation energies, $E_{\rm seg}(Sr_A')$, for the top eight layers of $LaMnO_3$ (001) slabs: filled blue triangles represent the data of a 15-layer BO_2 terminated slab (two BO_2 surfaces), empty red triangles represent the data of a 15-layer AO terminated slab (two AO surfaces), and filled purple triangles represent the data of a 16-layer stoichiometric slab (with the BO_2 surface on the left and the AO surface on the right).

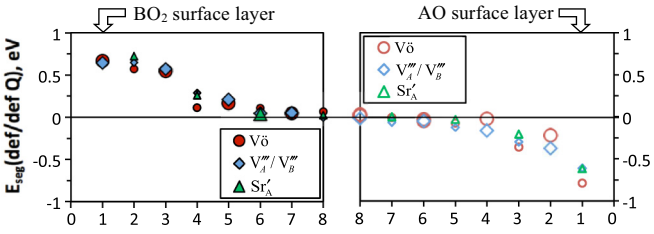

FIG. 18. (Color online) $LaMnO_3$ defect ($V\ddot{o}$: red circles; V_A'''/V_B''': blue diamonds; and Sr_A': green triangles) segregation energies normalized with formal charge of defects (-2, $+3$, and $+1$ for $V\ddot{o}$, V_A'''/V_B''', and Sr_A', respectively) of a 15-layer BO_2 terminated slab (left figure with filled symbols) and 15-layer AO terminated slab (right figure with empty symbols). Note the more stable $E_{seg}(V\ddot{o})$s of the two distinct O sites of each BO_2 layer (as shown in Fig. 15) are chosen to represent the $E_{seg}(V\ddot{o})$ of each plane.

level diagram for electron transfer in formation of $V\ddot{o}$ and $V_A'''/V_B'''/Sr_A'$ for the $LaMnO_3$ bulk and (001) AO and BO_2 surfaces to illustrate how $LaMnO_3$/LSM surface point defect segregation energies are influenced by shifts of the Fermi level

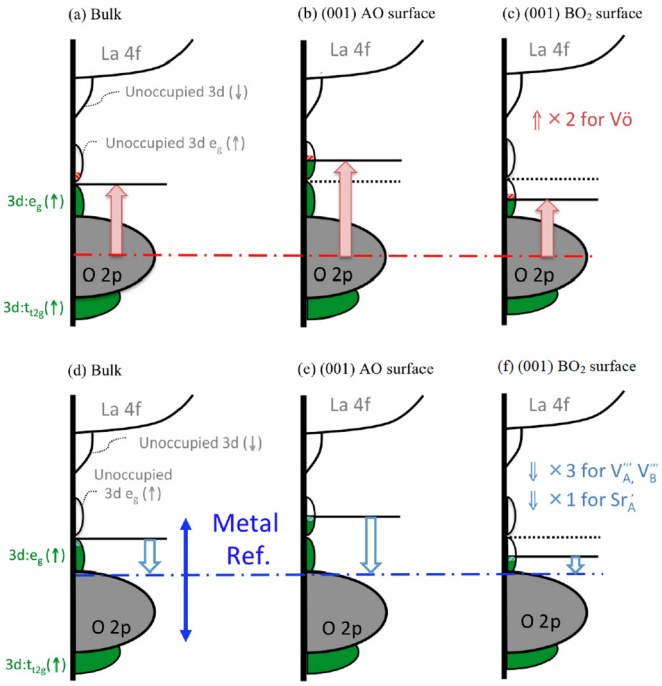

FIG. 19. (Color online) Energy level diagram for electron transfer in formation of (a) bulk $V\ddot{o}$, (b) (001) AO surface $V\ddot{o}$, (c) (001) BO_2 surface $V\ddot{o}$, (d) bulk $V_A'''/V_B'''/Sr_A'$, (e) (001) AO surface $V_A'''/V_B'''/Sr_A'$, and (f) (001) BO_2 surface $V_A'''/V_B'''/Sr_A'$ for the $LaMnO_3$ bulk and (001) AO and BO_2 surfaces. All energy is referenced to the O $2p$ band of the bulk and surface layers. The single arrows represent the energy of electron transfer in the point defect formation. The red and blue dash-dotted lines indicate the O $2p$ band center and the metal references of $LaMnO_3$. The metal references are not uniquely defined in perovskites (see discussions in Sec. II), and their range is indicated by the blue double arrow (only for guiding without quantitative meaning). The schematic plots shown here do not include band structure change due to surface relaxation and bond breaking.

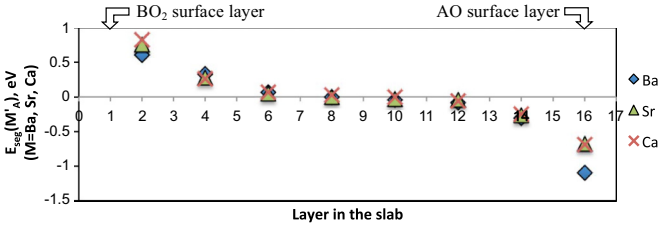

FIG. 20. (Color online) Surface dopant segregation energies (Ba_A': blue diamonds; Sr_A': green triangles; and Ca_A': red crosses) of the $LaMnO_3$ 16-layer (001) slab. Arrows indicate the location of top surface layers of the slab.

relative to the O $2p$ band of the surfaces (i.e., surface band bending). The doping of electrons (AO) and holes (BO_2) into the $3d$ e_g bands raise and lower the Fermi energy, respectively. The increased Fermi energy for the AO-terminated surfaces then destabilized the electron doping from $V\ddot{o}$ and stabilized the hole doping charge from $V_A'''/V_B'''/Sr_A'$. The decreased Fermi energy causes the opposite trend for the BO_2-terminated surfaces.

(d) Additional notes on dopant size effect for dopant segregation energies. In early and recent theoretical papers, it was proposed that the two fundamental factors governing defect and dopant segregation near grain boundaries and surfaces of oxides or ionic systems are electrostatic interaction and strain (elastic) energy [24,41,83,84]. Yan *et al.* [84] demonstrated that both electrostatic and elastic driving forces can be coupled for dopant segregation near grain boundaries of ionic solids, and one may be affected by the other under certain conditions. Recently, Lee *et al.* [24] investigated the oxygen partial pressure and temperature dependences for dopant segregation among the Ca_A', Sr_A', and Ba_A'-doped $LaMnO_3$ surfaces of epitaxial thin films on the $SrTiO_3$ substrate and suggest that cation size mismatch (strain) and charge interactions (electrostatics) are the main driving forces for the observed dopant segregation on Ca_A', Sr_A', and Ba_A'-doped $LaMnO_3$ surfaces vs temperature and oxygen partial pressure. To further understand the effect of strain energy relative to the surface polarity on the dopant segregation energetics, we vary the dopant size by replacing Sr with Ba and Ca to compare their E_{seg}s in the 16-layer $LaMnO_3$ stoichiometric (001) slab model, as shown in Fig. 20. Interestingly, almost identical E_{seg} vs slab layer location profiles are observed for all the three dopants, with that largest variation E_{seg}s at the surface layer. The E_{seg}s of the three dopant types at the top (001) AO surface layer in this paper are similar but lower (by $-0.3\sim-0.5$ eV) than those reported by Lee *et al.* [24], which could be due to the difference in the DFT modeling approaches for calculating surface segregation energy (i.e., in this paper we calculate dopant segregation energy based on Eq. 1, while in Ref. [24] the dopant segregation energy are calculated by explicitly taking the total energy difference of slabs vs the bulk, with the slab energy derived from averaging between the undoped $LaMnO_3$ and doped $LaMnO_3$ nine-layer slabs). Nonetheless, the trend of the AO surface E_{seg}s vs the dopant size shows good agreement with Ref. [24], and we would follow Lee *et al.* [24] in attributing the trend to surface strain relaxation

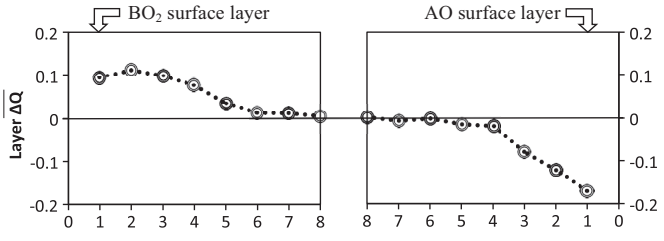

FIG. 21. Moving average of layer charge doping obtained from Bader charge analysis shown in Fig. 25(c) of the Appendix for $LaMnO_3$ (data based on the 15-layer symmetric slab model). The moving average of layer charge doping (ΔQ) is calculated by averaging the layer charge doping with it nearest-neighbor layers (one layer below and one layer above, except for the surface layers that only include one layer below).

associated with dopant size mismatch vs the host A-site cation.

Our result suggests that in the case of the ideal $LaMnO_3$ (001) surfaces with dilute dopants, the main driving force of the observed $LaMnO_3$ E_{seg} profile is due to the electrostatic interaction between the surface compensating charge originated from bulk polarity (which creates a strong electric field near the surfaces) and point defects (as well as the cation dopants), and surface strain relaxation leads to additional but secondary contribution to the top surface layer dopant segregation energies. We note upon increasing Ca'_A, Sr'_A, and Ba'_A dopant concentration in bulk $LaMnO_3$ (or in heavily doped $LaMnO_3$), the surface dipole effect will be reduced since both the AO and BO_2 layer charge is modified by the presence of the 2+ cation dopant in the AO layer and an increase of the TM valence in the BO_2 layer, and thereby reducing the total dipole moment and the surface compensating charge. Therefore, it is expected that with increasing Ca, Sr, and Ba 2+ cation dopant concentration, the elastic strain effect will become increasingly important relative to the electrostatic effect from charge interaction between surface charge and dopants and may be dominant over the surface polarity in heavily doped $LaMnO_3$.

Finally, it can be seen that the surface layer charge doping results of the $LaMnO_3$ (001) 15-layer and 16-layer slabs shown in Fig. 25(c) of the Appendix are not trivially correlated with the normalized defect segregation energy profiles shown in Fig. 18. In particular, the charges seem to fluctuate as one moves from the surface while the defect segregation energies are changing monotonically, and the charge appears to reach bulk values somewhat closer to the surface than the defect energies. However, one should remember that defining charge doping in this layer-by-layer manner is a specific choice to quantify charge changes and the defects may be responding to the average charge over multiple layers. In fact, by taking moving averages of layer charge doping with nearest-neighbor layers (shown in Fig. 21), it is seen that the moving average of the layer charge doping profile now resembles that of the normalized surface defect segregation energies. This result suggests that an average charge density of nearby layers is a more appropriate measure of local charge doping near the $LaMnO_3$ (001) surfaces than a single layer charge.

V. DISCUSSIONS

While $LaAlO_3$, $SrTiO_3$, and $LaMnO_3$ all belong to the perovskite family, in this paper we have shown that the three systems exhibit distinct behavior in surface charge, electrostatic potential profiles between the 16-layer asymmetric and 15-layer symmetric slab models, surface energies, and surface defect energetics for the unreconstructed (001) surfaces. These differences result from coupling of a number of factors but originate in the different surface dipole compensating charge (the role of bulk polarity) and the way that surface charge can be accommodated in these materials (the role of TM redox capability). Here we first summarize the key results for $LaMnO_3$ surface energy (Sec. V A) and surface defect energetics (Sec. V B) and then discuss the fundamental factors leading to distinct surface energy and surface defect chemistry for $LaMnO_3$ vs $LaAlO_3$ and $SrTiO_3$ in Sec. V C.

A. $LaMnO_3$ surface energy—short surface charge screening length and rapid surface energy convergence with slab thickness

In this paper, we show that for unreconstructed polar surfaces, $LaMnO_3$ (001) surfaces can screen the surface dipole compensating charge in a shorter length (∼3 unit cell depth) than $LaAlO_3$ and that consequently a bulklike region forms at a shallower depth when compared to the $LaAlO_3$. The bulklike region is illustrated by (1) convergence of surface energy vs slab thickness at thickness ∼4 unit cells (Sec. III D); (2) convergence of central-region layer DOS to bulk by ∼3 unit cell depth (Sec. III C 3); and (3) convergence of the defect energies to bulk values by ∼3 unit cell depth (Figs. 14–16 of %Sec. IV B 3). The ability to screen the surface charge with low-energy cost is expected to enable much more stable polar surfaces in TM mixed ionic-electronic conducting perovskites than more ionic perovskites. This hypothesis is consistent with the low $LaMnO_3$ (001) surface energy [which is close to that of $SrTiO_3$ (see Fig. 8)] and is also suggested by recent *ab initio* surface thermodynamic stability analysis [39,42]. For the more localized electronic characteristics of $LaAlO_3$, the large band gap creates a large energy penalty for surface metallization and leads to a much higher (001) surface energy than that of $LaMnO_3$.

The weakly polar $SrTiO_3$ (001) surfaces exhibit the lowest surface energy among the three systems (see Fig. 8), which is believed to be at least in part due to the weak polar nature of $SrTiO_3$, as bond breaking of the truncated (001) surfaces is sufficient to compensate for their weak polarity and only a small energy cost is paid to move charge around to compensate the dipole [e.g., metallization does not occur at the $SrTiO_3$ (001) surfaces]. Therefore, the surface energy of weakly polar $SrTiO_3$ exhibits weak or almost no thickness dependence. However, the presence of TiO_2 surface states causes Fermi level pinning of the whole slab to a higher energy level and leads to E_{Fermi} going from low to high in the following order: SrO-terminated 15-layer symmetric slab, 16-layer asymmetric slab, and TiO_2-terminated 15-layer symmetric slab. This trend in E_{Fermi} further causes a slightly split surface energy between the asymmetric and symmetric slab models. In other words, our results suggest that for the $SrTiO_3$ slab models containing the TiO_2 surfaces, there is still no bulklike region, despite no

additional surface charge being generated to compensate the weak polarity.

B. $LaMnO_3$ surface defect energetics—correlation between polar surface compensating charge doping and point defect segregation energies

For the unreconstructed $LaMnO_3$ (001) surfaces, our surface defect segregation energies suggest that the main driving force for surface defect segregation is governed by surface charge introduced by bulk polarity. We demonstrate that the profiles of $E_{seg}(V\ddot{o})$, $E_{seg}(V_A'''/V_B''')$, and $E_{seg}(Ca_A'/Sr_A'/Ba_A')$ vs the slab layer location of the $LaMnO_3$ (001) slab models collapse onto a single master curve when normalized with respect to the formal defect charge and are also highly correlated with the surface charge doping profile when it is properly averaged. In contrast, although polarity compensation also occurs in $LaAlO_3$ (001) surfaces, the non-TM $LaAlO_3$ perovskite exhibits no simple correlation between surface charge and surface defect segregation energies. This different behavior is due to the fact that there is much longer range electrostatic interaction in a more ioniclike system and that the large band gap leads dissimilar compensation for defects with the opposite charge vs the same charge relative to the charge of the polar surface. Specifically, strong segregation of defects with the opposite charge as the electron doping at the polar surface occurs in $LaAlO_3$, just as in $LaMnO_3$, but segregation of defects with the same charge as the electron doping at the polar surface remains close to the bulk value. Such distinction of surface defect energetics between the $LaMnO_3$ and $LaAlO_3$ (001) polar surfaces reflects the role of the redox active TM with an e_g orbital degeneracy in accommodating the same type of charge from strong polar surfaces and point defects: in $LaMnO_3$, the introduced charge from surface polarity compensation and the point defects interact through change of the d (or more specifically e_g) electron filling (i.e., TM redox), while in $LaAlO_3$ both the surface states and the defect states of point defects are localized and the surface states pins the Fermi level of the slabs. Therefore, creating a point defect with the same doping charge type as the polar surfaces does not alter the surface Fermi level relative to the band features (i.e., surface band bending). In Fig. 26 and Fig. 27 of the Appendix, we show the electrostatic profiles of the $V\ddot{o}$ containing 16-layer asymmetric slab vs the perfect slab (Fig. 26 for $V\ddot{o}$ at the BO_2 surfaces and Fig. 27 for $V\ddot{o}$ at the AO surfaces) to demonstrate the different electrostatic potential profile change when forming a surface point defect at the $LaMnO_3$ surfaces vs at the $LaAlO_3$ and $SrTiO_3$ surfaces.

The weakly polar $SrTiO_3$ (001) surfaces do not have significant surface electronic redistribution as compared to the bulk (i.e., surfaces remain insulating and are not metallized) and only contain minor dipole compensating charge from surface bond breaking. Although Ti is a TM and one would consider that changing valence state is at a lower energetic cost than the band insulator of $LaAlO_3$, it does not behave like $LaMnO_3$ because it does not have strongly polar (001) surfaces and has a charge transfer gap between the occupied O $2p$ band and the unoccupied d band due to the empty d shell configuration (d^0). We demonstrate that the defect segregation energies at the $SrTiO_3$ (001) surfaces are not strongly influenced by weak surface polarity and are instead governing by reduction of bond breaking (coordination number) in surface vs in bulk and the presence of TiO_2 surface states, which interact strongly with cation vacancies.

C. Factors leading to distinct $LaMnO_3$ surface properties

1. *Surface charge compensation due to bulk polarity*

Abundant studies and discussions on the surface/interface charge compensation (surface/interface electronic compensation) for strong polar perovskites can be found in the literature, and it is often described as the "polar catastrophe" [32,54,77,79,85–90]. Here this phenomenon is briefly summarized for the investigated perovskite systems. The formal charge in the perovskite layers cause $LaMnO_3$ and $LaAlO_3$ to be a strongly polar system where additional surface compensating charge is generated at the polar surfaces [see the slab layer Bader charge in Fig. 25 of the Appendix and Fig. 4 and Fig. 6 for the DOS of the $LaAlO_3$ and $LaMnO_3$ (001) slabs, respectively]. On the other hand, the charges in the perovskite layers cause $SrTiO_3$ to be only a weakly polar system, and a relatively small amount of surface charge is introduced locally due to surface bond breaking, which can sufficiently compensate for the weak polarity of the bulk without metallizing the surfaces [see the slab layer Bader charge in Fig. 25 of the Appendix and Fig. 5 for the DOS of the $SrTiO_3$ (001) slab]. As will be discussed below, the coupling between the surface compensating charge and the facile redox of the Mn^{3+} further leads to distinct $LaMnO_3$ surface energetics as compared to those of $LaAlO_3$.

2. *Roles of TMs with an e_g orbital degeneracy and the charge transfer gap for TMs with d^0 and d^5*

In this paper, we have shown the effective screening of surface compensating charge and point defects in $LaMnO_3$ through facile redox of Mn^{3+} (d^4), which leads to a bulklike region existing at lower slab thickness than $LaAlO_3$ and converged bulk point defect segregation energies between 15-layer symmetric and 16-layer asymmetric (001) slab models. In contrast, nonconverged surface energy and surface cation segregation energy in $SrTiO_3$ suggests a lack of screening of the weak surface charge by Ti^{4+} (d^0). To address distinct surface properties arising from varying the TM cations, here we discuss the roles of TM with partially filled e_g orbital occupation (which are generally used as solid oxide fuel cell cathode materials) in strong polar TM perovskite surface energetics and the role of the charge transfer gap in TM perovskite surfaces with d^0 and d^5 configurations.

(a) The role of TM with partial occupation of e_g orbital. The reduction and oxidation energetics of TM oxides are associated with the electronic structures near the Fermi level, which can be described by the TM-ligand field splitting, d-electron filling, and the degree of metal-oxygen hybridization [49,91]. In solid oxide fuel cell cathode applications, the TM-based mixed ionic-electronic conducting perovskites generally contain d shell configurations with a partially filled e_g band (e.g., $La_{1-x}Sr_xMnO_3$, $La_{1-x}Sr_xCoO_3$, $La_{1-x}Sr_xCo_{1-y}Fe_yO_3$, etc.). When the TM cation d-shell configurations contain a partially filled e_g band in the cubic perovskite symmetry, the e_g states are degenerate in their energy level and strongly interact with the O $2p$ states of coordinating oxygens, forming broad σ^*

bands [91]. Therefore, the Fermi level of these TM-based mixed ionic-electronic conducting perovskites at the cubic symmetry lies within the e_g band and can lead to metallic properties. It is noted that the e_g orbital degeneracy can be removed at lower symmetry, e.g., due to JT distortion, which results in a substantial gap between the occupied and unoccupied e_g states. Nonetheless, typical solid oxide fuel cell operating temperatures ($T =\sim 1000$ K) are above the orbital ordering transition temperature, and the solid oxide fuel cell perovskite materials are generally doped with aliovalent cations such as Sr^{2+} (which stabilizes the ferromagnetic phase), which together lead to the cubic or close-to-cubic symmetry. For example, the JT transition temperature is about 750 K for $LaMnO_3$ and above 750 K $LaMnO_3$ exhibits average cubic symmetry [92] and a significant reduction of the band gap vs the room temperature orthorhombic phase [70]. The availability of partially filled e_g states (or with small splitting energy between occupied and unoccupied e_g states) near the Fermi level allows accommodation of strong polar surface compensating charge and surface defect charge at low-energy cost by shifting the surface Fermi level within the available e_g states relative to the core electron level or the vacuum level. This process leads to effective screening of the electrostatic field near the polar surfaces of the slabs and a relatively low thickness requirement for converged surface properties (i.e., slabs become bulklike after just a few layers).

An exception to the above situation is for the partial e_g orbital occupation with a half-filled d-shell (d^5) configuration (with e_g occupation equal to two) in the cubic perovskite symmetry. This configuration does not lead to metallic behavior due to strong d-electron exchange interaction (the penalty for pairing d electrons in the same orbital) [93], which splits the majority and minority spin states and leads to a large charge transfer gap, such as seen in $LaFeO_3$ (~2 eV band gap) [93,94]. The existence of a charge transfer gap can further lead to distinct surface properties from the mixed electronic-ionic conducting perovskites, as will be further discussed below.

(b) Charge transfer gap for TM perovskites with d^0 and d^5. The discussion in this section addresses the TM perovskites with d shell configurations containing zero or weak ligand field splitting (i.e., d^0 and d^5 configurations), which share similar features with non-TM oxides. For these systems the top of the filled valence band is predominantly composed of the O $2p$ band [93] and a substantial charge transfer gap exists between the filled valence band and the unoccupied conduction band (typical band gaps are 2–4 eV) [94,95]. The existence of a charge transfer gap creates a significant electron chemical potential contribution in surface defect energetics through Fermi level pinning by the surface states at the polar surfaces vs the bulk, which shifts the surface Fermi level close to the CBM and VBM or within the band gap (depending on the energy level of the surface states). As shown previously in the $LaAlO_3$ surface energies vs slab thickness and surface defect energetics, the screening of the electrostatic field caused by the surface dipole in strong polar perovskites with a large band gap is less effective as compared to those of LMO. We therefore expect that the TM-based strong polar perovskites with empty or half-filled d shell can exhibit similar surface energetics to those shown previously in the $LaAlO_3$ system due to a large charge transfer gap.

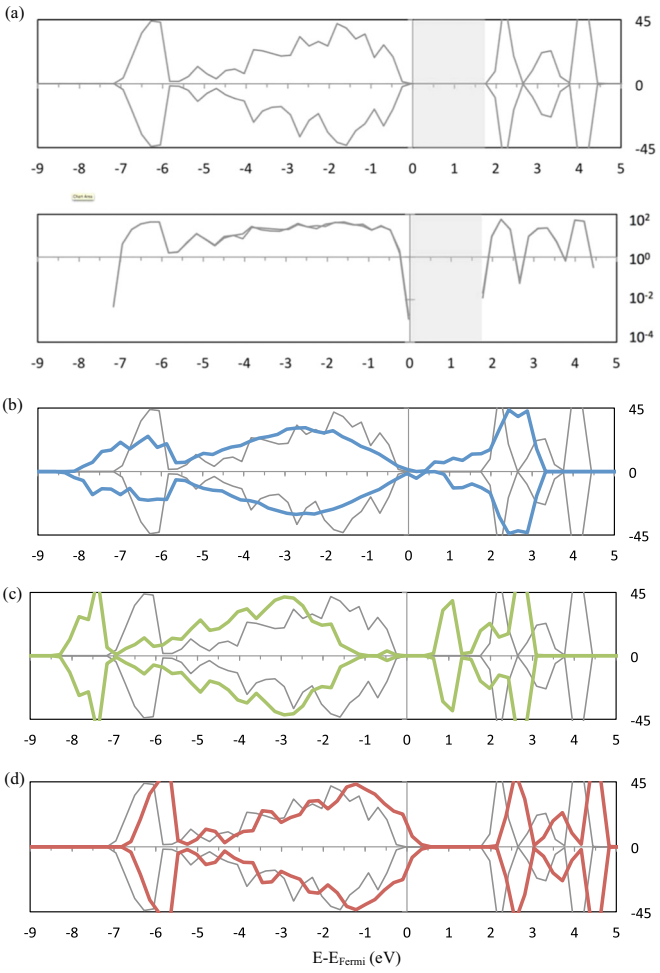

FIG. 22. (Color online) Plots of calculated DOS for $LaFeO_3$ (a) G-type antiferromagnetic bulk, (b) asymmetric 14-layer slab, (c) symmetric 15-layer AO-terminated slab, and (d) symmetric 15-layer BO_2-terminated slab. In plot (a), the upper plot is the DOS with y axis in the absolute scale, and the lower plot is the DOS with y axis in the logarithm scale. The shaded area represents the size of the band gap. In plots (b), (c), and (d), thick and thin solid lines represent the slab and the bulk DOS respectively, and the Fermi energy level is aligned at zero.

For example, the antiferromagnetic $LaFeO_3$ exhibits a ~2 eV band gap [94], which is consistent with the high-energy cost for redox of the Fe^{3+} (half-filled d shell, d^5), and this large gap means the surface properties of ideal polar antiferromagnetic $LaFeO_3$ (001) surfaces may behave similar to $LaAlO_3$. To assess this claim we show in Fig. 22 the DOS of $LaFeO_3$ G-type antiferromagnetic bulk (nearest-neighbor Fe antiferromagnetic coupling) and 14-layer asymmetric and 15-layer symmetric (001) slab models calculated using the same slab modeling approach as $LaMnO_3$ with the $U_{\text{eff}} = 4$ eV for the Fe $3d$ electrons [36,64]. It is seen that the spreading (covering more range of energies) of the band structures of the 14-layer asymmetric (001) slab vs bulk is similar to the DOS plot of $LaAlO_3$ shown in Fig. 4(a), as expected from the fact that both have a significant band gap (the calculated G-type antiferromagnetic $LaFeO_3$ has a band gap of ~1.8 eV). However, we note that there is a smearing (less sharp peaks

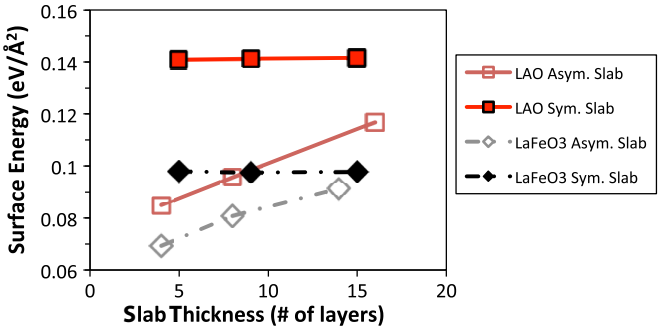

FIG. 23. (Color online) Calculated surface energy of the (001) slabs vs slab thickness for $LaAlO_3$ (red squares) and $LaFeO_3$ (grey diamonds). Data of asymmetric slabs and symmetric slabs are plotted with solid and empty symbols, respectively. The lines connecting the data shown in the plot are guides to the eye.

in the DOS) of band features in the DOS plots of the 15-layer symmetric slab models [Figs. 22(b) and 22(c)] that occurs in $LaFeO_3$ but is not seen in $LaAlO_3$. These smearings originate from band bending between the surface layer and the central region of the slab and show that there is more band bending in $LaFeO_3$ than $LaAlO_3$. Another similarity between $LaFeO_3$ and $LaAlO_3$ can be seen in Fig. 23, which shows the calculated (001) surface energy of the *G*-type antiferromagnetic $LaFeO_3$ vs slab thickness. It is seen in Fig. 23 that the $LaFeO_3$ surface energy thickness dependence is similar to that of $LaAlO_3$, suggesting that the thickness of the simulated $LaFeO_3$ (001) slab models is insufficient to provide a converged bulklike region. Both *G*-type antiferromagnetic $LaFeO_3$ (001) slab DOS and surface energy results suggest that the role of band gap in the *G*-type antiferromagnetic $LaFeO_3$ may lead to surface properties more similar to $LaAlO_3$ than $LaMnO_3$. However, by introducing sufficient Sr and Co doping in $LaFeO_3$, acceptor states are introduced to the VBM, and the ferromagnetic arrangement is promoted [96], and hence removing or adding charge will take place using the available e_g states close to the Fermi level. Thus we expect that the surface properties of heavily Sr and Co doped $LaFeO_3$ may behave more similarly to $LaMnO_3$/LSM than to $LaAlO_3$. In fact, most mixed ionic-electronic conducting perovskites in solid oxide fuel cell applications contain either the TM elements such as Mn, Co, Ni with smaller band gaps and facile redox, or high doping content, or both. Therefore, we believe that the qualitative trends shown in this paper for $LaMnO_3$ are expected to hold for polar mixed ionic-electronic conducting perovskites, which will generally be quite different from the weakly polar $SrTiO_3$ and non-TM $LaAlO_3$. However, the quantitative values of properties such as surface charge screening lengths, surface energies, and surface defect energetics, will likely depend on the specific system being studied.

VI. CONCLUSIONS

In this paper, we perform a comparative study for $LaMnO_3$, $LaAlO_3$, and $SrTiO_3$ (001) surfaces and surface defect energetics based on *ab initio* modeling. Despite the structural similarity, it is demonstrated that unreconstructed (001) surfaces of $LaMnO_3$ (TM polar perovskite with the Mn d^4 configuration) are chemically quite distinct from those of $LaAlO_3$ (non-TM polar perovskite) and $SrTiO_3$ (TM non-polar perovskite with an empty *d* shell). Specifically, we have shown major differences in their surface charge, electrostatic potential profile normal to the surfaces of the slabs, surface electronic structure, location of dipole compensating charge, surface energy thickness dependence, and surface defect energetics. These differences have been explained in terms of the presence or absence of a surface dipole and a redox active TM with partial e_g orbital occupation in the system. Overall, our comparative study highlights that coupling of the TM cation redox abilities originated from short-range metal-ligand field interactions and *d*-electron fillings, and long-range electrostatic interactions can result in distinct surface chemistry for perovskite oxides. We also demonstrate how surfaces of mixed ionic-electronic conducting perovskite oxides are fundamentally different from those of polar non-TM ($LaAlO_3$) and nonpolar TM perovskites with an empty *d* shell ($SrTiO_3$). In addition, we show for the case of $LaMnO_3$ ideal (001) surfaces with dilute Sr/Ba/Ca doping that the dopant segregation energy profile is mainly governed by interaction between dopants and the surface compensating charge near the polar surfaces. Nonetheless, upon increasing Sr/Ba/Ca doping, it is expected that the elastic (strain) effect may become increasingly important or even dominant over the electrostatic effect from surface polarity due to reduction of the layer charge (the slab dipole moment). Although real surfaces could deviate from the ideal surface models used in the *ab initio* modeling, we believe that the same fundamental factors will still play an important role in the perovskite surface chemistry even in the presence of other reconstructions. These different surface chemistries are a fundamental piece of understanding for rational design of perovskite oxides for solid oxide fuel cell cathodes and other applications, e.g., oxygen permeation membranes.

ACKNOWLEDGMENTS

We gratefully acknowledge financial support from U.S. Department of Energy (U.S. DOE), Office of Basic Energy Sciences, Division of Materials Sciences and Engineering (under Award No. DE-SC0001284). We also gratefully acknowledge computing support from a National Energy Research Scientific Computing Center (NERSC) allocation from the Center for Nanophase Materials Sciences (CNMS) (under Grant No. CNMS2013-292), which is sponsored at Oak Ridge National Laboratory by the Division of Scientific User Facilities, U.S. Department of Energy. This paper also benefitted from the use of the Extreme Science and Engineering Discovery Environment (XSEDE), which is supported by National Science Foundation Grant No. OCI-1053575.

APPENDIX

1. Bulk DOS plots of $LaAlO_3$, $SrTiO_3$, $LaMnO_3$ calculated with a 3 × 3 × 3 *k*-point mesh.

Figure 24 in this Appendix provides higher resolution DOS plots for the bulk systems being studied.

2. Bader charge doping of layers for $LaAlO_3$, $SrTiO_3$, and $LaMnO_3$ (001) surfaces

Figure 25 shows calculated charge changes of each layer (surface layer charge relative to the bulk layer charge) for

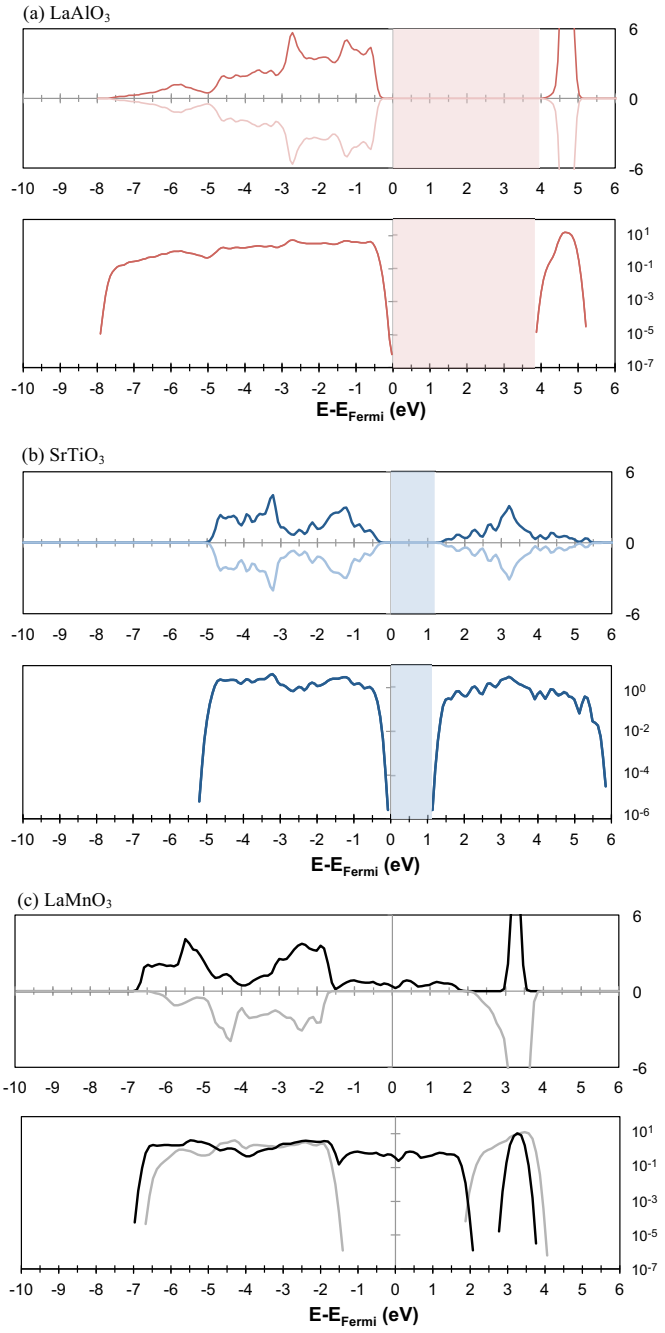

FIG. 24. (Color online) Plots of calculated total DOS, normalized per formula unit, for bulk (a) $LaAlO_3$, (b) $SrTiO_3$, and (c) $LaMnO_3$ with a $3 \times 3 \times 3$ k-point mesh. For each material system, two sets of DOS plots with different y axis presentation are included. The upper plot gives absolute y axis with positive numbers for up-spin states and negative numbers for down-spin states, and the lower plot gives the logarithm scale y axis with dark color for the up-spin states and light color for down-spin states. The logarithm scale plots exclude zero states in the DOS and allows one to easily distinguish systems with and without band gaps. In each plot, the Fermi energy level is aligned at zero, and the shaded area represents the size of the band gap.

$LaAlO_3$, $SrTiO_3$, and $LaMnO_3$ (001) surfaces based on Bader charge analysis [67]. Our $LaAlO_3$ and $SrTiO_3$ surface charge results are in agreement with previous theoretical

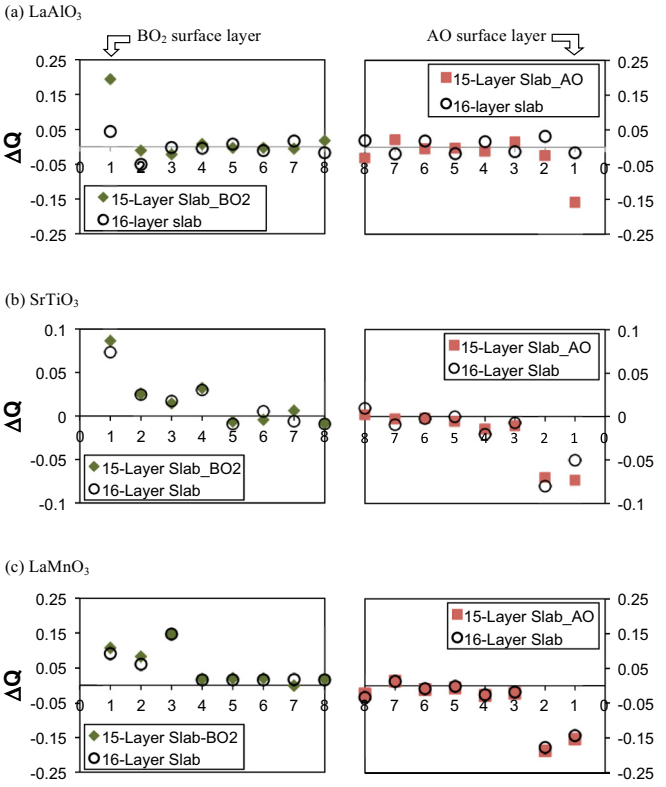

FIG. 25. (Color online) Charge doping, ΔQ, in each layer of the (001) slabs for the perovskite (a) $LaAlO_3$, (b) $SrTiO_3$, and (c) $LaMnO_3$. Charge doping is calculated in terms of the Bader charge of each layer of the slab relative to the bulk layer.

works [54,75,76] except that overall the Bader charge analysis in this paper exhibits a smaller magnitude of charge density changes as compared to the results of Mulliken charge analysis.

In Fig. 25, it is seen that all of the $LaAlO_3$, $SrTiO_3$, and $LaMnO_3$ (001) surfaces are charge doped, with holes created near the BO_2 surfaces and electrons formed near the AO surfaces, except for the $LaAlO_3$ 16-layer asymmetric slab model. For strong polar 15-layer symmetric (001) slab systems, e.g., $LaAlO_3$ and $LaMnO_3$, an extra AO plane has formal charge $+1$ (all charges are measured in units of electrons) and therefore effectively gives up one electron and donates it to the system, creating an n-type system. Similarly, an extra BO_2 (AlO_2 or MnO_2) plane has a formal charge -1 and therefore donates one hole to the system, creating a p-type system. The excess charge created due to nonstoichiometry is $+1$ (-1) in a symmetric BO_2 (AO) terminated slab and is exactly the right magnitude and sign of charge doping needed for surface compensation of Tasker's type 3 polar surfaces [32,79]. To understand this relationship better, we note that the charge compensation mechanism of Tasker's type 3 polar surfaces requires surface layer charge, $\sigma_{\text{surf\_layer}}$, equal to negative half of the bulk atomic layer charge, $\sigma_{\text{bulk\_layer}}$ [79]. Thus for a BO_2 (AO) terminated surface the compensating charge doping is $+0.5$ (-0.5). For a symmetric slab with two identical surfaces, the compensating charge needed for BO_2 (AO) terminated slabs is $+1$ (-1), exactly the amount of extra charge created due to nonstoichiometry. Such balancing means that the symmetric slab calculations not only have no net dipole (due to their

symmetry) but also have excess charge doping available to compensate their polar surfaces in exactly the same way as would be compensated in the high thickness limit. Therefore, for even a moderate number of layers, the surfaces in the symmetric slab model can be considered to be a good approximation to the case of surfaces in the thick film limit [32,85].

The layer Bader charge of the 16-layer slab asymmetric model is very close to the bulk layer charge, which indicates that electronic compensation (introduction of extra surface compensating charge) does not occur as the main surface stabilization mechanism to accommodate the total dipole moment of the $LaAlO_3$ (001) 16-layer slab. Instead, the dipole moment has been found to lead to lattice polarization to screen the electrical field in the slab and slight charge transfer between the AO and BO_2 surfaces [54,77]. The different (001) surface charge between the $LaAlO_3$ 15-layer symmetric slab and the 16-layer asymmetric slab models further results in distinct surface energies and defect energetics between the two slab models, as discussed in Sec. III D and Sec. IV B of the main text.

In the case of weak polar $SrTiO_3$ (001) surfaces, the similarity of layer charge doping between the 16-layer asymmetric and 15-layer symmetric slab models can be attributed to the fact that surface bond breaking on its own is sufficient to compensate the weak polarity [32], and thereby the surface charge doping is mainly a result of local bond breaking near the surface region instead of a macroscopic dipole effect. Nonetheless, slight layer charge differences are observed in Fig. 25(b) of the Appendix for the top surface layer between the 16-layer asymmetric and 15-layer symmetric slab models, suggesting that a certain degree of electronic redistribution between the two surfaces may still occur in the asymmetric slab models.

For the $LaMnO_3$ (001) surfaces, both 16-layer asymmetric and 15-layer symmetric slab models exhibit almost identical surface charge doping, as shown in Fig. 25(c) of the Appendix. That the layer charge of $LaMnO_3$ (001), the 16-layer symmetric slab, is similar to that of 15-layer symmetric slabs suggests that the $LaMnO_3$ (001) 16-layer slab model has extra surface charge introduced to the (001) surfaces to

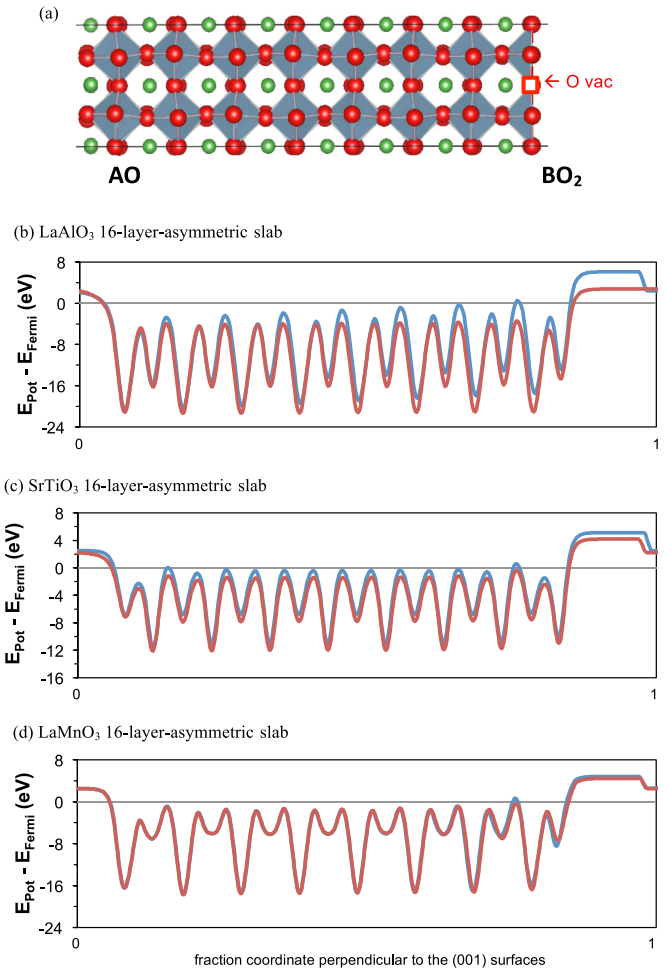

FIG. 26. (Color online) (a) 16-layer asymmetric slab model and (b) $LaAlO_3$, (c) $SrTiO_3$, and (d) $LaMnO_3$ electrostatic potential (relative to the Fermi level of the slabs) profiles along the direction perpendicular to the surfaces of the (001) slab models for the perovskite. The blue lines are the electrostatic potential profiles of the perfect 16-layer asymmetric slab models, while the red lines are electrostatic potential profile of the oxygen vacancy containing 16-layer asymmetric slabs, respectively. The location of the oxygen vacancy in the 16-layer asymmetric slab is in the surface BO_2 layer on the right hand side and is also specified with a red square in the schematic, shown in (a).

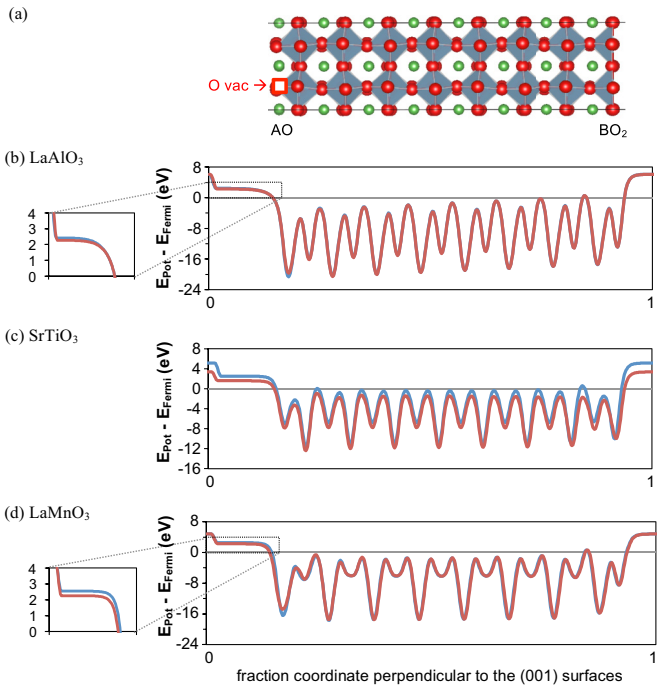

FIG. 27. (Color online) (a) 16-layer asymmetric slab model and (b) $LaAlO_3$, (c) $SrTiO_3$, and (d) $LaMnO_3$ electrostatic potential (relative to the Fermi level of the slabs) profiles along the direction perpendicular to the surfaces of the (001) slab models for the perovskite. The blue lines are the electrostatic potential profiles of the perfect 16-layer asymmetric slab models, while the red lines are electrostatic potential profile of the oxygen vacancy containing 16-layer asymmetric slabs, respectively. The location of the oxygen vacancy in the 16-layer asymmetric slab is in the surface AO layer on the left hand side and is also specified with a red square in the schematic shown in (a). A zoom-in subplot on the left of the main plot for $LaAlO_3$ (and $LaMnO_3$) shows the clear distinction of the electrostatic potential profiles near the AO surface.

accommodate the total dipole moment of the slab, which is in contrast to $LaAlO_3$, where the total dipole moment of the 16-layer (001) slab is stabilized by lattice polarization and does not contain significant surface compensating charge. Such difference in surface charge compensation between the $LaMnO_3$ and $LaAlO_3$ 16-layer (001) slabs reflects the fact that the facile redox of Mn in $LaMnO_3$ allows it to accommodate extra charge doping at low-energy cost, while introducing charge to $LaAlO_3$ is energetically unfavorable and therefore surface stabilization with charge is substituted by lattice polarization in the slab at low thickness.

3. Electrostatic potential profiles for $LaAlO_3$, $SrTiO_3$, and $LaMnO_3$ (001) surfaces with an oxygen vacancy

In this Appendix section, the electrostatic profiles of the $V\ddot{o}$ containing 16-layer asymmetric slab vs the perfect slab for $V\ddot{o}$ at the BO_2 surfaces and at the AO surfaces are shown in Fig. 26 and Fig. 27, respectively. Different electrostatic potential profile change can be observed when forming a surface point defect at the $LaMnO_3$ surfaces vs at the $LaAlO_3$ and $SrTiO_3$ surfaces.

4. Symmetric vs asymmetric slab models

The different chemistry of $LaMnO_3$ vs $LaAlO_3$ has implications for how *ab initio* calculations must be used to study these types of systems. Calculations of surface properties of $LaMnO_3$ are fairly well converged when slab thickness exceeds the distance needed for screening the surface dipole compensating charge, which occurs relatively quickly with respect to number of layers (∼7–8 layers). Therefore, with sufficient slab thickness to screen the surface compensating charge, both the asymmetric and symmetric slab models will have almost identical surface energies and surface defect energetics. On the other hand, in the more ionic $LaAlO_3$ with longer range electrostatic interaction and more localized electrons, the surface properties are sensitive to the number of layers and surfaces present for any presently practical cell size, unless the compensating charge is explicitly added to the system. Specifically, the two types of the (001) slab models, asymmetric (stoichiometric) and symmetric (nonstoichiometric) slabs, exhibit different surface stability thickness dependence. Interaction between the two counter surfaces remains in the $LaAlO_3$ stoichiometric slabs up to eight unit cell thickness (extrapolation of surface energy vs thickness for $LaAlO_3$ asymmetric and symmetric slab models suggests crossover occurs at ∼26 layers or ∼13 unit cells of thickness). The nonstoichiometry of the symmetric slab forces surface charge equal to half of the bulk layer charge and gives rise to higher surface energy with no thickness dependence. Surprisingly, interactions (electron redistribution) between the two counter surfaces also occurs in the 16-layer asymmetric slab of the weakly polar $SrTiO_3$, which leads to distinct cation vacancy segregation energies between the symmetric and asymmetric slab models as well as the nonconverged surface energy. Therefore, researchers must choose surfaces carefully to properly represent the physics of interest. To model a thin-film system, the correct surfaces of the actual system must be used to properly account for how dipole surface compensation occurs when surfaces can interact. To model a thick film, where one surface should be independent of the other, symmetric slabs can be used, as they naturally provide the compensating charge that would otherwise come from the large bulklike region of a thick film.

[1] B. C. H. Steele, Survey of materials selection for ceramic fuel cells. 2. Cathodes and anodes, Solid State Ion. **86–88**, 1223 (1996).

[2] S. B. Adler, Factors governing oxygen reduction in solid oxide fuel cell cathodes, Chem. Rev. **104**, 4791 (2004).

[3] S. C. Singhal and K. Kendall, *High Temperature Solid Oxide Fuel Cells: Fundamentals, Design and Applications*, 1st ed. (Elsevier Science, Oxford, U.K., 2003).

[4] J. A. Kilner, R. A. De Souza, and I. C. Fullarton, Surface exchange of oxygen in mixed conducting perovskite oxides, Solid State Ion. **86–88**, 703 (1996).

[5] R. A. De Souza and J. A. Kilner, Oxygen transport in $La_{1-x}Sr_xMn_{1-y}Co_yO_{3\pm\delta}$ perovskites part II. Oxygen surface exchange, Solid State Ion. **126**, 153 (1999).

[6] Y.-L. Lee, J. Kleis, J. Rossmeisl, Y. Shao-Horn and D. Morgan, Prediction of solid oxide fuel cell cathode activity with first-principles descriptors, Energy Environ. Sci. **4**, 3966 (2011).

[7] J. H. Kuo, H. U. Anderson, and D. M. Sparlin, Oxidation-reduction behavior of undoped and Sr-doped $LaMnO_3$: Defect structure, electrical conductivity, and thermoelectric power, J. Solid State Chem. **87**, 55 (1990).

[8] J. Nowotny and M. Rekas, Defect chemistry of (La, Sr)MnO_3, J. Am. Ceram. Soc. **81**, 67 (1998).

[9] J. Fleig, Solid oxide fuel cell cathodes: Polarization mechanisms and modeling of the electrochemical performance, Annu. Rev. Mater. Res. **33**, 361 (2003).

[10] J. H. Kuo, H. U. Anderson, and D. M. Sparlin, Oxidation-reduction behavior of undoped and sr-doped $LaMnO_3$: Nonstoichiometry and defect structure, J. Solid State Chem. **83**, 52 (1989).

[11] J. A. M. van Roosmalen and E. H. P. Cordfunke, The defect chemistry of $LaMnO_{3+\delta}$: 5. Thermodynamics, J. Solid State Chem. **110**, 113 (1994).

[12] F. W. Poulsen, Defect chemistry modelling of oxygen-stoichiometry, vacancy concentrations, and conductivity of $(La_{1-x}Sr_x)_yMnO_{3\pm\delta}$, Solid State Ion. **129**, 145 (2000).

[13] J. Mizusaki, N. Mori, H. Takai, Y. Yonemura, H. Minamiue, H. Tagawa, M. Dokiya, H. Inaba, K. Naraya, T. Sasamoto and T. Hashimoto, Oxygen nonstoichiometry and defect equilibrium in the perovskite-type oxides $La_{1-x}Sr_xMnO_{3+\delta}$, Solid State Ion. **129**, 163 (2000).

[14] D. S. Mebane, Y. J. Liu, and M. L. Liu, Refinement of the bulk defect model for $La_xSr_{1-x}MnO_{3\pm\delta}$, Solid State Ion. **178**, 1950 (2008).

[15] Y.-L. Lee and D. Morgan, *Ab initio* and empirical defect modeling of $LaMnO_{3\pm\delta}$ for solid oxide fuel cell cathodes, Phys. Chem. Chem. Phys. **14**, 290 (2012).

[16] P. Decorse, G. Caboche, and L. C. Dufour, A comparative study of the surface and bulk properties of lanthanum-strontium-manganese oxides $La_{1-x}Sr_xMnO_{3\pm\delta}$ as a function of Sr-content, oxygen potential and temperature, Solid State Ion. **117**, 161 (1999).

[17] H. Dulli, P. A. Dowben, S.-H. Liou, and E. W. Plummer, Surface segregation and restructuring of colossal-magnetoresistant manganese perovskites $La_{0.65}Sr_{0.35}MnO_3$, Phys. Rev. B **62**, R14629(R) (2000).

[18] Q. H. Wu, M. L. Liu, and W. Jaegermann, X-ray photoelectron spectroscopy of $La_{0.5}Sr_{0.5}MnO_3$, Mater. Lett. **59**, 1480 (2005).

[19] N. Caillol, M. Pijolat, and E. Siebert, Investigation of chemisorbed oxygen, surface segregation and effect of post-treatments on $La_{0.8}Sr_{0.2}MnO_3$ powder and screen-printed layers for solid oxide fuel cell cathodes, Appl. Surf. Sci. **253**, 4641 (2007).

[20] T. T. Fister, D. D. Fong, J. A. Eastman, P. M. Baldo, M. J. Highland, P. H. Fuoss, K. R. Balasubramaniam, J. C. Meador, and P. A. Salvador, *In situ* characterization of strontium surface segregation in epitaxial $La_{0.7}Sr_{0.3}MnO_3$ thin films as a function of oxygen partial pressure, Appl. Phys. Lett. **93**, 151904 (2008).

[21] G. J. la O', R. F. Savinell, and Y. Shao-Horn, Activity enhancement of dense strontium-doped lanthanum manganite thin films under cathodic polarization: A combined AES and XPS study, J. Electrochem. Soc. **156**, B771 (2009).

[22] K. Katsiev, B. Yildiz, K. Balasubramaniam, and P. A. Salvador, Electron tunneling characteristics on $La_{0.7}Sr_{0.3}MnO_3$ thin-film surfaces at high temperature, Appl. Phys. Lett. **95**, 092106 (2009).

[23] L. F. J. Piper, A. R. H. Preston, S.-W. Cho, A. DeMasi, B. Chen, J. Laverock, K. E. Smith, L. J. Miara, J. N. Davis, S. N. Basu, U. Pal, S. Gopalan, L. Saraf, T. Kaspar, A. Y. Matsuura, P.-A. Glans, and J.-H. Guo, Soft X-Ray spectroscopic study of dense strontium-doped lanthanum manganite cathodes for solid oxide fuel cell applications, J. Electrochem. Soc. **158**, B99 (2011).

[24] W. Lee, J. W. Han, Y. Chen, Z. Cai, and B. Yildiz, Cation size mismatch and charge interactions drive dopant segregation at the surfaces of manganite perovskites, J. Am. Chem. Soc. **135**, 7909 (2013).

[25] W. A. Harrison, Origin of Sr segregation at $La_{1-x}S_xMnO_3$ surfaces, Phys. Rev. B **83**, 155437 (2011).

[26] H. Jalili, J. W. Han, Y. Kuru, Z. Cai, and B. Yildiz, New insights into the strain coupling to surface chemistry, electronic structure, and reactivity of $La_{0.7}Sr_{0.3}MnO_3$, J. Phys. Chem. Lett. **2**, 801 (2011).

[27] B. Puchala, Y.-L. Lee, and D. Morgan, A-Site diffusion in $La_{1-x}Sr_xMnO_3$: *Ab Initio* and kinetic Monte Carlo calculations, J. Electrochem. Soc. **160**, F877 (2013).

[28] G. J. la O', S.-J. Ahn, E. Crumlin, Y. Orikasa, M. D. Biegalski, H. M. Christen and Y. Shao-Horn, Catalytic activity enhancement for oxygen reduction on epitaxial perovskite thin films for solid-oxide fuel cells, Angew. Chem. Int. Ed. **49**, 5344 (2010).

[29] E. J. Crumlin, E. Mutoro, Z. Liu, M. E. Grass, M. D. Biegalski, Y.-L. Lee, D. Morgan, H. M. Christen, H. Bluhm, and Y. Shao-Horn, Surface strontium enrichment on highly active perovskites for oxygen electrocatalysis in solid oxide fuel cells, Energy Environ. Sci. **5**, 6081 (2012).

[30] M. E. Lynch, L. Yang, W. Qin, J.-J. Choi, M. Liu, K. Blinn and M. Liu, Enhancement of $La_{0.6}Sr_{0.4}Co_{0.2}Fe_{0.8}O_{3-\delta}$ durability and surface electrocatalytic activity by $La_{0.85}Sr_{0.15}MnO_{3\pm\delta}$ investigated using a new test electrode platform, Energy Environ. Sci. **4**, 2249 (2011).

[31] D. Oh, D. Gostovic, and E. D. Wachsman, Mechanism of $La_{0.6}Sr_{0.4}Co_{0.2}Fe_{0.8}O_3$ cathode degradation, J. Mater. Res. **27**, 1992 (2012).

[32] J. Goniakowski, F. Finocchi, and C. Noguera, Polarity of oxide surfaces and nanostructures, Rep. Prog. Phys. **71**, 016501 (2008).

[33] C. H. Lanier, J. M. Rondinelli, B. Deng, R. Kilaas, K. R. Poeppelmeier, and L. D. Marks, Surface reconstruction with a fractional hole: $(\sqrt{5}\times\sqrt{5})R26.6^\circ$ $LaAlO_3$ (001), Phys. Rev. Lett. **98**, 086102 (2007).

[34] A. A. Knizhnik, I. M. Iskandarova, A. A. Bagatur'yants, B. V. Potapkin, L. R. C. Fonseca, and A. Korkin, First-principles calculations of the electrical properties of $LaAlO_3$ and its interface with Si, Phys. Rev. B **72**, 235329 (2005).

[35] N. Erdman, K. R. Poeppelmeier, M. Asta, O. Warschkow, D. E. Ellis, and L. D. Marks, The structure and chemistry of the TiO_2-rich surface of $SrTiO_3$(001), Nature **419**, 55 (2002).

[36] Y.-L. Lee, J. Kleis, J. Rossmeisl, and D. Morgan, *Ab initio* energetics of $LaBO_3$(001) (B = Mn, Fe, Co, and Ni) for solid oxide fuel cell cathodes, Phys. Rev. B **80**, 224101 (2009).

[37] Y.-L. Lee and D. Morgan, Prediction of surface oxygen vacancy concentrations of $(La_{1-x}Sr_x)MnO_3$, ECS Trans. **25**, 2769 (2009).

[38] E. A. Kotomin, Y. A. Mastrikov, E. Heifets, and J. Maier, Adsorption of atomic and molecular oxygen on the $LaMnO_3$(001) surface: *Ab initio* supercell calculations and thermodynamics, Phys. Chem. Chem. Phys. **10**, 4644 (2008).

[39] S. Piskunov, E. Heifets, T. Jacob, E. A. Kotomin, D. E. Ellis, and E. Spohr, Electronic structure and thermodynamic stability of $LaMnO_3$ and $La_{1-x}Sr_xMnO_3$ (001) surfaces: *Ab initio* calculations, Phys. Rev. B **78**, 121406(R) (2008).

[40] A. Kushima, S. Yip, and B. Yildiz, Competing strain effects in reactivity of $LaCoO_3$ with oxygen, Phys. Rev. B **82**, 115435 (2010).

[41] H. Ding, A. V. Virkar, M. Liu, and F. Liu, Suppression of Sr surface segregation in $La_{1-x}Sr_xCo_{1-y}Fe_yO_{3-\delta}$: A first principles study, Phys. Chem. Chem. Phys. **15**, 489 (2013).

[42] Yu. A. Mastrikov, E. Heifets, E. A. Kotomin, and J. Maier, Atomic, electronic and thermodynamic properties of cubic and orthorhombic $LaMnO_3$ surfaces, Surf. Sci. **603**, 326 (2009).

[43] S. Piskunov, T. Jacob, and E. Spohr, Oxygen adsorption at $La_{1-x}Sr_xMnO_3$ (001) surfaces: Predictions from first principles, Phys. Rev. B **83**, 073402 (2011).

[44] K. Fuchigami, Z. Gai, T. Z. Ward, L. F. Yin, P. C. Snijders, E. W. Plummer, and J. Shen, Tunable metallicity of the $La_{5/8}Ca_{3/8}MnO_3$ (001) surface by an oxygen overlayer, Phys. Rev. Lett. **102**, 066104 (2009).

[45] S. Rößler, B. Padmanabhan, S. Elizabeth, H. L. Bhat, F. Steglich, and S. Wirth, Atomically resolved scanning tunneling microscopy on perovskite manganite single crystals, Appl. Phys. Lett. **96**, 202512 (2010).

[46] B. Bryant, Ch. Renner, Y. Tokunaga, Y. Tokura, and G. Aeppli, Imaging oxygen defects and their motion at a manganite surface, Nat. Commun. **2**, 212 (2011).

[47] Z. Feng, Y. Yacoby, W. T. Hong, H. Zhou, M. D. Biegalski, H. M. Christen, and Y. Shao-Horn, Revealing the atomic structure and strontium distribution in nanometer-thick $La_{0.8}Sr_{0.2}CoO_{3-\delta}$-grown on (001)-oriented $SrTiO_3$, Energy Environ. Sci. **7**, 1166 (2014).

[48] J. Suntivich, H. A. Gasteiger, N. Yabuuchi, H. Nakanishi, J. B. Goodenough, and Y. Shao-Horn, Design principles for oxygen-reduction activity on perovskite oxide catalysts for fuel cells and metal–air batteries, Nat. Chem. **3**, 546 (2011).

[49] J. Suntivich, K. J. May, H. A. Gasteiger, J. B. Goodenough, and Y. Shao-Horn, A Perovskite oxide optimized for oxygen evolution catalysis from molecular orbital principles, Science **334**, 1383 (2011).

[50] I. C. Man, H.-Y. Su, F. Calle-Vallejo, H. A. Hansen, J. I. Martínez, N. G. Inoglu, J. Kitchin, T. F. Jaramillo, J. K. Nørskov, and J. Rossmeisl, Universality in oxygen evolution electrocatalysis on oxide surfaces, ChemCatChem **3**, 1159 (2011).

[51] R. A. Evarestov, E. A. Kotomin, D. Fuks, J. Felsteiner, and J. Maier, *Ab initio* calculations of the $LaMnO_3$ surface properties, Appl. Surf. Sci. **238**, 457 (2004).

[52] J. Padilla and D. Vanderbilt, *Ab initio* study of $SrTiO_3$ surfaces, Surf. Sci. **418**, 64 (1998).

[53] J. Carrasco, F. Illas, N. Lopez, E. A. Kotomin, Y. F. Zhukovskii, R. A. Evarestov, Y. A. Mastrikov, S. Piskunov, and J. Maier, First-principles calculations of the atomic and electronic structure of F centers in the bulk and on the (001) surface of $SrTiO_3$, Phys. Rev. B **73**, 064106 (2006).

[54] H. Seo and A. A. Demkov, First-principles study of polar LaAlO (001) surface stabilization by point defects, Phys. Rev. B **84**, 045440 (2011).

[55] E. A. Kotomin, R. A. Evarestov, Yu. A. Mastrikov, and J. Maier, DFT plane wave calculations of the atomic and electronic structure of $LaMnO_3$(001) surface, Phys. Chem. Chem. Phys. **7**, 2346 (2005).

[56] G. Kresse and J. Hafner, *Ab initio* molecular dynamics for liquid metals, Phys. Rev. B **47**, 558 (1993).

[57] G. Kresse and J. Furthmuller, Efficient iterative schemes for *ab initio* total-energy calculations using a plane-wave basis set, Phys. Rev. B **54**, 11169 (1996).

[58] P. E. Blochl, Projector augmented-wave method, Phys. Rev. B **50**, 17953 (1994).

[59] G. Kresse and D. Joubert, From ultrasoft pseudopotentials to the projector augmented-wave method, Phys. Rev. B **59**, 1758 (1999).

[60] J. P. Perdew and Y. Wang, Accurate and simple analytic representation of the electron-gas correlation energy, Phys. Rev. B **45**, 13244 (1992).

[61] S. Geller and V. B. Bala, Crystallographic studies of perovskite-like compounds. II. Rare earth alluminates, Acta. Crystallogr. **9**, 1019 (1956).

[62] N. Furuhata, E. Nakamura, and E. Sawaguchi, *Landolt-Börnstein, Group III 3* (Springer-Verlag, Berlin, 1969).

[63] J. F. Mitchell, D. N. Argyriou, C. D. Potter, D. G. Hinks, J. D. Jorgensen, and S. D. Bader, Structural phase diagram of $La_{1-x}Sr_xMnO_{3+\delta}$: Relationship to magnetic and transport properties, Phys. Rev. B **54**, 6172 (1996).

[64] L. Wang, T. Maxisch, and G. Ceder, Oxidation energies of transition metal oxides within the GGA + U framework, Phys. Rev. B **73**, 195107 (2006).

[65] F. Calle-Vallejo, J. I. Martínez, J. M. García-Lastra, M. Mogensen, and J. Rossmeisl, Trends in Stability of Perovskite Oxides, Angew. Chem. Int. Ed. **49**, 7699 (2010).

[66] A. Jain, G. Hautier, C. J. Moore, S. Ping Ong, C. C. Fischer, T. Mueller, K. A. Persson, and G. Ceder, A high-throughput infrastructure for density functional theory calculations, Comput. Mater. Sci. **50**, 2295 (2011).

[67] R. F. W. Bader, *Atoms in Molecules—a Quantum Theory* (Clarendon Press, Oxford, UK, 1994).

[68] G. Makov and M. C. Payne, Periodic boundary-conditions in *ab-initio* calculations, Phys. Rev. B **51**, 4014 (1995).

[69] J. Neugebauer and M. Scheffler, Adsorbate-substrate and adsorbate-adsorbate interactions of Na and K adlayers on Al(111), Phys. Rev. B **46**, 16067 (1992).

[70] K. Tobe, T. Kimura, Y. Okimoto, and Y. Tokura, Anisotropic optical spectra in a detwinned $LaMnO_3$ crystal, Phys. Rev. B **64**, 184421 (2001).

[71] J. Töpfer and J. B. Goodenough, $LaMnO_{3+\delta}$ Revisited, J. Solid State Chem. **130**, 117 (1997).

[72] X. Luo, B. Wang, and Y. Zheng, First-principles study on energetics of intrinsic point defects in $LaAlO_3$, Phys. Rev. B **80**, 104115 (2009).

[73] T. Tanaka, K. Matsunaga, Y. Ikuhara, and T. Yamamoto, First-principles study on structures and energetics of intrinsic vacancies in $SrTiO_3$, Phys. Rev. B **68**, 205213 (2003).

[74] K. Johnston, M. R. Castell, A. T. Paxton, and M. W. Finnis, $SrTiO_3$(001)(2 × 1) reconstructions: First-principles calculations of surface energy and atomic structure compared with scanning tunneling microscopy images, Phys. Rev. B **70**, 085415 (2004).

[75] E. Heifets, R. I. Eglitis, E. A. Kotomin, J. Maier, and G. Borstel, First-principles calculations for $SrTiO_3$(100) surface structure, Surf. Sci. **513**, 211 (2002).

[76] J.-L. Tang, J. Zhu, W.-F. Qin, J. Xiong, Y. Zhang, and Y.-R. Li, Atomic relaxation and electronic redistribution of $LaAlO_3$(001) surfaces, Phys. Lett. A **365**, 149 (2007).

[77] R. Pentcheva and W. E. Pickett, Avoiding the Polarization Catastrophe in $LaAlO_3$ Overlayers on $SrTiO_3$ (001) through Polar Distortion, Phys. Rev. Lett. **102**, 107602 (2009).

[78] A. Baldereschi, S. Baroni, and R. Resta, Band offsets in lattice-matched heterojunctions: A model and first-principles calculations for GaAs/AlAs, Phys. Rev. Lett. **61**, 734 (1988).

[79] P. W. Tasker, Stability of ionic-crystal surfaces, J. Phys. C **12**, 4977 (1979).

[80] N. A. Richter, S. Sicolo, S. V. Levchenko, J. Sauer, and M. Scheffler, Concentration of vacancies at metal-oxide surfaces: Case study of MgO(100), Phys. Rev. Lett. **111**, 045502 (2013).

[81] K. Xiong, J. Robertson, and S. J. Clark, Defect states in the high-dielectric-constant gate oxide $LaAlO_3$. Appl. Phys. Lett. **89**, 022907 (2006).

[82] H. Lu, T. A. George, Y. Wang, I. Ketsman, J. D. Burton, C.-W. Bark, S. Ryu, D. J. Kim, J. Wang, C. Binek, P. A. Dowben, A. Sokolov, C.-B. Eom, E. Y. Tsymbal, and A. Gruverman, Electric modulation of magnetization at the $BaTiO_3/La_{0.67}Sr_{0.33}MnO_3$ interfaces, Appl. Phys. Lett. **100**, 232904 (2012).

[83] W. D. Kingery, Plausible Concepts Necessary and Sufficient for Interpretation of Ceramic Grain-Boundary Phenomena: II, Solute Segregation, Grain-Boundary Diffusion, and General Discussion*, J. Am. Ceram. Soc. **57**, 74 (1974).

[84] M. F. Yan, R. M. Cannon, and H. K. Bowen, Space charge, elastic field, and dipole contributions to equilibrium solute segregation at interfaces, J. Appl. Phys. **54**, 764 (1983).

[85] H. Chen, A. M. Kolpak, and S. Ismail-Beigi, Electronic and magnetic properties of $SrTiO_3/LaAlO_3$ interfaces from first principles, Adv. Mater. **22**, 2881 (2010).

[86] N. C. Bristowe, E. Artacho, and P. B. Littlewood, Oxide superlattices with alternating p and n interfaces, Phys. Rev. B **80**, 045425 (2009).

[87] A. Ohtomo and H. Y. Hwang, A high-mobility electron gas at the $LaAlO_3/SrTiO_3$ heterointerface, Nature **427**, 423 (2004).

[88] N. Nakagawa, H. Y. Hwang, and D. A. Muller, Why some interfaces cannot be sharp, Nat. Mater. **5**, 204 (2006).

[89] M. Stengel and D. Vanderbilt, Berry-phase theory of polar discontinuities at oxide-oxide interfaces, Phys. Rev. B **80**, 241103 (2009).

[90] M. Stengel, First-principles modeling of electrostatically doped perovskite systems, Phys. Rev. Lett. **106**, 136803 (2011).

[91] J. B. Goodenough, Electronic and ionic transport properties and other physical aspects of perovskites, Rep. Prog. Phys. **67**, 1915 (2004).

[92] J. Rodriguez-Carvajal, M. Hennion, F. Moussa, A. H. Moudden, L. Pinsard, and A. Revcolevschi, Neutron-diffraction study of the Jahn-Teller transition in stoichiometric $LaMnO_3$, Phys. Rev. B **57**, R3189 (1998).

[93] M. Abbate, F. M. F. Degroot, J. C. Fuggle, A. Fujimori, O. Strebel, F. Lopez, M. Domke, G. Kaindl, G. A. Sawatzky, M. Takano, Y. Takeda, H. Eisaki, and S. Uchida, Controlled-valence properties of $La_{1-x}Sr_xFeO_3$ and $La_{1-x}Sr_xMnO_3$ studied by soft-x-ray absorption-spectroscopy, Phys. Rev. B **46**, 4511 (1992).

[94] T. Arima, Y. Tokura, and J. B. Torrance, Variation of optical gaps in perovskite-type 3d transition-metal oxides, Phys. Rev. B **48**, 17006 (1993).

[95] H. W. Eng, P. W. Barnes, B. M. Auer, and P. M. Woodward, Investigations of the electronic structure of d^0 transition metal oxides belonging to the perovskite family, J. Solid State Chem. **175**, 94 (2003).

[96] V. G. Sathe, S. K. Paranjpe, V. Siruguri, and A. V. Pimpale, Novel magnetic phases in $La_{0.7}Sr_{0.3}Co_{1-y}Fe_yO_3$ ($0.0 \leqslant y \leqslant 1.0$): A neutron diffraction study, J. Phys.: Condens. Matter **10**, 4045 (1998).